

Birefringence and polarized luminescence of the manganese(II) chloride–triphenylphosphine oxide compound: application in LED and photolithography

Alexey Berezin

Nikolaev Institute of Inorganic Chemistry, Siberian Branch of Russian Academy of Sciences, Acad. Lavrentiev Ave. 3, Novosibirsk 630090, Russian Federation. E-mail: berezin-1991@ngs.ru, berezin@niic.nsc.ru

Experimental part

Synthesis of $[(\text{Ph}_3\text{PO})_2\text{MnCl}_2]$ (**1**)

Solid $\text{MnCO}_3 \cdot \text{xH}_2\text{O}$ (44–46 % Mn, 28.8 mg, 0.250 mmol) and Ph_3PO (139.1 mg, 0.500 mmol) were dissolved separately in warm hydrochloric acid HCl (37% HCl, 1.0 ml, 50°C), and the solutions were mixed. The mixture was evaporated at 50°C down to approximately 0.3 ml volume. Then, warm ethanol (97% EtOH, 4 ml, 50°C) was added, and the mixture was stirred at 50°C for 1 h with gradual cooling down to 20°C for 3 h. Crystals formed on the surface of the glassware. Yield: 137 mg (80% Mn); greenish-yellow crystals.

Solid $\text{MnCl}_2 \cdot 4\text{H}_2\text{O}$ (49.5 mg, 0.250 mmol) and Ph_3PO (139.1 mg, 0.500 mmol) were dissolved separately in warm ethanol (97% EtOH, 4 ml, 50°C), and the solutions were mixed. Next, warm hydrochloric acid HCl (37% HCl, 0.2 ml, 50°C) was introduced into the mixture followed by stirring at 50°C for 3 h with gradual cooling down to 20°C for 3 h. Crystals formed on the surface of the glassware. Yield: 130 mg (76% Mn); greenish-yellow crystals.

Methods

Single-crystal X-ray data were collected at 150 K on a Bruker X8 single-crystal diffractometer with a graphite monochromator ($\lambda(\text{Mo}K_\alpha) = 0.71073 \text{ \AA}$, ω -scans) using an Oxford Cryosystems Cryostream 800 Plus open-flow nitrogen cooler and a Bruker D8 Venture single-crystal diffractometer (Incoatec I μ S 3.0 microfocus X-ray source with Mo-anode, 3-circle goniometer, PHOTON III C14 CPAD detector). Apex3 v.2018–7.2 software¹ was used for unit cell determination, calculation of the data acquisition strategy, integration, and absorption correction. The obtained hkl datasets were processed in Olex2 v.1.5 software² along with SHELXT³ for structure solution and SHELXL⁴ for subsequent refinement. All non-hydrogen atoms were refined anisotropically. The crystallographic data and details of the structure refinements are summarized in Tables S1–S4. CCDC 2177623 contains the supplementary crystallographic data for this paper. These data can be obtained free of charge from The Cambridge Crystallographic Data Center at http://www.ccdc.cam.ac.uk/data_request/cif.

Corrected luminescence spectra were recorded on a Fluorolog 3 spectrometer (Horiba Jobin Yvon) with a cooled PC177CE-010 photon detection module equipped with an R2658 photomultiplier, with continuous 450 W and pulsed (pulse time FWHM 3 μs) 50 W Xe-lamps, and with two Czerny–Turner double monochromators. Absolute values of quantum yields were determined using the Quanta- ϕ device of Fluorolog 3. Temperature dependences of luminescence were studied using an Optistat DN optical cryostat (Oxford Instruments). The luminescence quantum yield at 77 K was obtained relative to the quantum yield of the same sample at 300 K.⁵ Corrected polarization luminescence spectra were acquired on the Fluorolog 3 spectrometer equipped with the two rotated linear polarizers. A film of **1** was prepared on a quartz substrate from a hydrochloric acid/ethanol solution (1:1) (concentration of **1**: 10^{-4} mmol/ml) by the spin-coating method at 5000 rpm for 30 min at 300 K.

The light-emitting diodes (LED) TO-3535BC-UVC265-30-6V-E with $\lambda_{\max} = 275 \text{ nm}$ were used for the fabrication of a portable light emitter based on **1**. The LED was modified by a film of **1** coated on the LED surface from the ethanol solution. Also, the LED was modified by single crystals of **1** placed on the LED surface.

EPR spectra were recorded on a Varian E-109 spectrometer in X- and Q-bands at 300 K. A 2,2-diphenyl-1-picrylhydrazyl (DPPH) standard sample was employed to calibrate the magnetic field of the spectrometer. The spectra were simulated in MATLAB (The MathWorks Inc., Natick, MA, USA) using the EasySpin software for EPR data.⁶

Powder X-ray diffraction patterns were determined in the 6–40° 2 θ range using a Bruker D8 Advance powder diffractometer (vertical 0–0 goniometer in Bragg-Brentano geometry configuration, Cu-anode sealed tube with no β -filter 40mA @ 40 kV, LYNXEYE XE-T compound silicon strip detector, motorized divergence slit).

Structures of the complexes **1** and **1nl** were optimized by the spin-unrestricted DFT method using the Amsterdam density functional^{7, 8} software in the 3D band^{9, 10} approximation with gradient exchange functional GGA (BP86—Becke¹¹ and Perdew^{12, 13}), and the triple zeta polarized (TZP) basis set was used. Initial positions of atoms and unit cell parameters were taken from the X-ray structural analysis for **1** and CCDC DEGGIF10 for **1nl**. Frequency analysis was carried out to check the nature of stationary points (BP86, TZP). The \mathcal{G} -tensors¹⁴ were calculated via the Spin-Orbit ZORA^{15–17} approximation with hybrid functional PBE0.^{18, 19} Zero-field splitting (ZFS) parameters were obtained with the method proposed by van Wüllen and coworkers.^{20, 21} Electronic excitations were computed by the TD-DFT method^{22, 23} (CAM-B3LYP functional²⁴, TZP) and additionally with the spin-flip approximation.^{25, 26} The quantum theory of atoms in molecules (QTAIM),²⁷ the extended transition state method with natural orbitals for chemical valence theory (ETS-NOCV), and non-covalent interaction calculations^{28–34} were utilized to analyze non-covalent interactions in the ADF software (BP86, TZP).

1 APEX3 (v.2018-7.2). Madison, Wisconsin, USA: Bruker AXS Inc.; 2018.

2 O. V. Dolomanov, L. J. Bourhis, R. J. Gildea, J. A. K. Howard and H. Puschmann, OLEX2: A complete structure solution, refinement and analysis program, *Journal of Applied Crystallography*, 2009, **42**, 339–341, 10.1107/S0021889808042726.

3 G. M. Sheldrick, SHELXT - Integrated space-group and crystal-structure determination, *Acta Crystallographica Section A: Foundations of Crystallography*, 2015, **71**, 3–8, 10.1107/S2053273314026370.

4 G. M. Sheldrick, Crystal structure refinement with SHELXL, *Acta Crystallographica Section C: Structural Chemistry*, 2015, **71**, 3–8, 10.1107/S2053229614024218.

- 5 A. V. Artem'Ev, M. P. Davydova, A. S. Berezin, M. R. Ryzhikov and D. G. Samsonenko, Dicopper(I) Paddle-Wheel Complexes with Thermally Activated Delayed Fluorescence Adjusted by Ancillary Ligands, *Inorganic Chemistry*, 2020, **59**, 10699-10706, 10.1021/acs.inorgchem.0c01171.
- 6 S. Stoll and A. Schweiger, EasySpin, a comprehensive software package for spectral simulation and analysis in EPR, *J. Magn. Reson.*, 2006, **178**, 42-55, 10.1016/j.jmr.2005.08.013.
- 7 G. te Velde, F. M. Bickelhaupt, E. J. Baerends, C. Fonseca Guerra, S. J. A. van Gisbergen, J. G. Snijders and T. Ziegler, Chemistry with ADF, *J. Comput. Chem.*, 2001, **22**, 931-967, 10.1002/jcc.1056.
- 8 ADF 2022.1, SCM, Theoretical Chemistry, Vrije Universiteit, Amsterdam, The Netherlands, <http://www.scm.com>.
- 9 G. Te Velde and E. J. Baerends, Precise density-functional method for periodic structures, *Physical Review B*, 1991, **44**, 7888-7903, 10.1103/PhysRevB.44.7888.
- 10 BAND 2022.1, SCM, Theoretical Chemistry, Vrije Universiteit, Amsterdam, The Netherlands, <http://www.scm.com>.
- 11 A. D. Becke, Density-functional exchange-energy approximation with correct asymptotic behavior, *Physical Review A*, 1988, **38**, 3098-3100, 10.1103/PhysRevA.38.3098.
- 12 J. P. Perdew, Density-functional approximation for the correlation energy of the inhomogeneous electron gas, *Physical Review B*, 1986, **33**, 8822-8824, 10.1103/PhysRevB.33.8822.
- 13 J. P. Perdew, Erratum: Density-functional approximation for the correlation energy of the inhomogeneous electron gas (Physical Review B (1986) 34, 10 (7406)), *Physical Review B*, 1986, **34**, 7406, 10.1103/PhysRevB.34.7406.
- 14 E. Van Lenthe, P. E. S. Wormer and A. Van Der Avoird, Density functional calculations of molecular g-tensors in the zero-order regular approximation for relativistic effects, *J. Chem. Phys.*, 1997, **107**, 2488-2498, 10.1063/1.474590.
- 15 E. Van Lenthe, E. J. Baerends and J. G. Snijders, Relativistic regular two-component Hamiltonians, *The Journal of Chemical Physics*, 1993, **99**, 4597-4610, 10.1063/1.466059.
- 16 E. Van Lenthe, E. J. Baerends and J. G. Snijders, Relativistic total energy using regular approximations, *The Journal of Chemical Physics*, 1994, **101**, 9783-9792, 10.1063/1.467943.
- 17 E. Van Lenthe, Geometry optimizations in the zero order regular approximation for relativistic effects, *J. Chem. Phys.*, 1999, **110**, 8943-8953, 10.1063/1.478813.
- 18 S. Grimme, Accurate description of van der Waals complexes by density functional theory including empirical corrections, *J. Comput. Chem.*, 2004, **25**, 1463-1473, 10.1002/jcc.20078.
- 19 M. Ernzerhof and G. E. Scuseria, Assessment of the Perdew-Burke-Ernzerhof exchange-correlation functional, *J. Chem. Phys.*, 1999, **110**, 5029-5036, 10.1063/1.478401.
- 20 C. Van Wüllen, Magnetic anisotropy from density functional calculations. Comparison of different approaches: Mn₁₂O₁₂ acetate as a test case, *J. Chem. Phys.*, 2009, **130**, 10.1063/1.3134430.
- 21 S. Schmitt, P. Jost and C. Van Wullen, Zero-field splittings from density functional calculations: Analysis and improvement of known methods, *J. Chem. Phys.*, 2011, **134**, 10.1063/1.3590362.
- 22 S. J. A. Van Gisbergen, J. G. Snijders and E. J. Baerends, Implementation of time-dependent density functional response equations, *Computer Physics Communications*, 1999, **118**, 119-138, 10.1016/S0010-4655(99)00187-3.
- 23 F. Wang and T. Ziegler, A simplified relativistic time-dependent density-functional theory formalism for the calculations of excitation energies including spin-orbit coupling effect, *J. Chem. Phys.*, 2005, **123**, 10.1063/1.2061187.
- 24 T. Yanai, D. P. Tew and N. C. Handy, A new hybrid exchange-correlation functional using the Coulomb-attenuating method (CAM-B3LYP), *Chem. Phys. Lett.*, 2004, **393**, 51-57, 10.1016/j.cplett.2004.06.011.
- 25 F. Wang and T. Ziegler, Time-dependent density functional theory based on a noncollinear formulation of the exchange-correlation potential, *J. Chem. Phys.*, 2004, **121**, 12191-12196, 10.1063/1.1821494.
- 26 F. Wang and T. Ziegler, The performance of time-dependent density functional theory based on a noncollinear exchange-correlation potential in the calculations of excitation energies, *J. Chem. Phys.*, 2005, **122**, 10.1063/1.1844299.
- 27 R. F. W. Bader, A Quantum Theory of Molecular Structure and Its Applications, *Chem. Rev.*, 1991, **91**, 893-928, 10.1021/cr00005a013.
- 28 M. P. Mitoraj, A. Michalak and T. Ziegler, A combined charge and energy decomposition scheme for bond analysis, *Journal of Chemical Theory and Computation*, 2009, **5**, 962-975, 10.1021/ct800503d.
- 29 J. I. Rodríguez, An efficient method for computing the QTAIM topology of a scalar field: The electron density case, *J. Comput. Chem.*, 2013, **34**, 681-686, 10.1002/jcc.23180.
- 30 J. I. Rodríguez, R. F. W. Bader, P. W. Ayers, C. Michel, A. W. Götz and C. Bo, A high performance grid-based algorithm for computing QTAIM properties, *Chem. Phys. Lett.*, 2009, **472**, 149-152, 10.1016/j.cplett.2009.02.081.
- 31 E. R. Johnson, S. Keinan, P. Mori-Sánchez, J. Contreras-García, A. J. Cohen and W. Yang, Revealing noncovalent interactions, *J. Am. Chem. Soc.*, 2010, **132**, 6498-6506, 10.1021/ja100936w.

- 32 J. Contreras-García, E. R. Johnson, S. Keinan, R. Chaudret, J. P. Piquemal, D. N. Beratan and W. Yang, NCIPILOT: A program for plotting noncovalent interaction regions, *Journal of Chemical Theory and Computation*, 2011, **7**, 625-632, 10.1021/ct100641a.
- 33 M. Aarabi, S. Gholami and S. J. Grabowski, S–H...O and O–H...O Hydrogen Bonds—Comparison of Dimers of Thiocarboxylic and Carboxylic Acids, *Chemphyschem*, 2020, **21**, 1653–1664, 10.1002/cphc.202000131.
- 34 J. Poater, M. Gimferrer and A. Poater, Covalent and Ionic Capacity of MOFs to Sorb Small Gas Molecules, *Inorganic Chemistry*, 2018, **57**, 6981–6990, 10.1021/acs.inorgchem.8b00670.

Table S1. X-Ray crystallographic data for **1**.

Empirical formula	C ₃₆ H ₃₀ Cl ₂ MnO ₂ P ₂
Formula weight	682.38
Temperature/K	150.00
Crystal system	monoclinic
Space group	P2 ₁ /n
a/Å	18.1040(6)
b/Å	10.1744(3)
c/Å	19.4063(5)
α/°	90
β/°	115.6240(10)
γ/°	90
Volume/Å ³	3223.03(17)
Z	4
ρ _{calc} g/cm ³	1.406
μ/mm ⁻¹	0.707
F(000)	1404.0
Crystal size/mm ³	0.114 × 0.083 × 0.082
Radiation	MoKα (λ = 0.71073)
2Θ range for data collection/°	4.082 to 66.354
Index ranges	-27 ≤ h ≤ 24, -15 ≤ k ≤ 15, -29 ≤ l ≤ 29
Reflections collected	43485
Independent reflections	12282 [R _{int} = 0.0348, R _{sigma} = 0.0398]
Data/restraints/parameters	12282/0/388
Goodness-of-fit on F ²	1.022
Final R indexes [I>=2σ (I)]	R ₁ = 0.0352, wR ₂ = 0.0766
Final R indexes [all data]	R ₁ = 0.0520, wR ₂ = 0.0826
Largest diff. peak/hole / e Å ⁻³	0.38/-0.30

Table S2. Fractional Atomic Coordinates (×10⁴) and Equivalent Isotropic Displacement Parameters (Å²×10³) for **1**. U_{eq} is defined as 1/3 of the trace of the orthogonalised U_{LL} tensor.

Atom	x	y	z	U(eq)
Mn01	2442.4(2)	2809.9(2)	5177.9(2)	14.09(4)
Cl02	2969.0(2)	1161.0(3)	4684.5(2)	24.08(7)
P003	2560.9(2)	5852.0(3)	4419.9(2)	14.49(6)
Cl04	1026.8(2)	2688.4(3)	4730.4(2)	24.66(7)
P005	3717.8(2)	2894.4(3)	7133.4(2)	17.80(7)
O006	2723.3(5)	4612.1(9)	4883.4(5)	19.64(18)
O007	3054.7(6)	2854.5(10)	6328.5(5)	24.2(2)
C008	2178.8(7)	5481.4(12)	3418.0(7)	16.6(2)
C009	3489.6(7)	6769.3(12)	4667.5(7)	17.2(2)
C00A	1829.2(7)	6871.7(12)	4557.2(7)	16.5(2)
C00B	3338.8(8)	3583.5(13)	7768.7(7)	21.1(2)
C00C	1666.6(8)	8164.1(13)	4284.6(8)	20.0(2)
C00D	1385.1(8)	6325.7(13)	4924.1(8)	20.6(2)
C00E	2184.7(8)	6428.4(13)	2900.8(8)	22.7(3)
C00F	3669.8(8)	7910.9(12)	5105.5(8)	20.3(2)
C00G	4115.4(8)	1285.8(12)	7476.3(7)	19.9(2)
C00H	1861.5(8)	4234.0(13)	3149.3(8)	22.5(3)
C00I	630.7(8)	8340.3(14)	4739.6(8)	24.3(3)
C00J	3691.1(9)	4693.2(14)	8210.0(8)	26.2(3)

C00K	784.2(8)	7062.6(14)	5007.3(8)	23.6(3)
C00L	5359.8(8)	3638.8(13)	7754.8(8)	23.0(3)
C00M	4433.5(9)	4879.0(14)	6661.7(8)	26.1(3)
C00N	4569.6(8)	3869.2(12)	7190.1(7)	19.9(2)
C00O	6007.8(9)	4397.3(14)	7782.9(8)	27.2(3)
C00P	1564.0(9)	3950.1(14)	2373.7(8)	26.2(3)
C00Q	2658.9(9)	2996.2(16)	7802.5(8)	28.8(3)
C00R	4985.9(9)	8034.5(15)	5079.7(9)	27.9(3)
C00S	1889.8(9)	6134.6(14)	2128.7(8)	26.2(3)
C00T	4468.2(9)	580.4(14)	7078.7(9)	28.4(3)
C00U	4416.7(8)	8541.7(13)	5304.5(8)	24.5(3)
C00V	1073.8(8)	8897.3(13)	4381.9(8)	23.9(3)
C00W	1582.4(9)	4891.4(15)	1866.3(8)	26.0(3)
C00X	4069.1(8)	6261.0(14)	4441.1(9)	26.4(3)
C00Y	5871.0(9)	5388.7(15)	7252.7(9)	30.1(3)
C00Z	3361.5(10)	5205.2(16)	8682.3(9)	32.5(3)
C010	5088.1(10)	5638.8(15)	6698.9(9)	31.6(3)
C011	2348.0(9)	3504.3(18)	8289.0(9)	33.8(3)
C012	4797.0(10)	-654.9(15)	7331.8(10)	33.0(3)
C013	4814.3(9)	6892.0(17)	4651.3(10)	32.4(3)
C014	2695.5(10)	4602.4(17)	8721.4(9)	33.3(3)
C015	4085.3(10)	731.8(15)	8118.8(8)	28.7(3)
C016	4403.3(11)	-520.2(17)	8360.5(9)	36.1(4)
C017	4763.8(9)	-1200.1(15)	7973.6(10)	34.3(3)

Table S3. Bond Lengths for **1**.

Atom	Atom	Length / Å
Mn01	Cl02	2.3301(4)
Mn01	Cl04	2.3264(4)
Mn01	O006	2.0491(9)
Mn01	O007	2.0189(9)
P003	O006	1.5027(9)
P003	C008	1.7993(13)
P003	C009	1.7972(12)
P003	C00A	1.7910(12)
P005	O007	1.5036(10)
P005	C00B	1.7927(13)
P005	C00G	1.7958(13)
P005	C00N	1.7964(14)
C008	C00E	1.3947(17)
C008	C00H	1.3977(18)
C009	C00F	1.3921(18)
C009	C00X	1.4000(18)
C00A	C00C	1.4003(17)
C00A	C00D	1.3989(17)
C00B	C00J	1.3938(19)
C00B	C00Q	1.395(2)
C00C	C00V	1.3854(18)
C00D	C00K	1.3868(18)
C00E	C00S	1.3883(19)
C00F	C00U	1.3920(18)
C00G	C00T	1.3944(19)
C00G	C015	1.3909(19)
C00H	C00P	1.3921(19)
C00I	C00K	1.383(2)
C00I	C00V	1.389(2)
C00J	C00Z	1.393(2)
C00L	C00N	1.3952(18)
C00L	C00O	1.385(2)
C00M	C00N	1.3961(18)

C00M	C010	1.390(2)
C00O	C00Y	1.385(2)
C00P	C00W	1.384(2)
C00Q	C011	1.391(2)
C00R	C00U	1.381(2)
C00R	C013	1.384(2)
C00S	C00W	1.387(2)
C00T	C012	1.386(2)
C00X	C013	1.3866(19)
C00Y	C010	1.382(2)
C00Z	C014	1.384(2)
C011	C014	1.375(2)
C012	C017	1.388(2)
C015	C016	1.393(2)
C016	C017	1.375(2)

Table S4. Bond Angles for **1**.

Atom	Atom	Atom	Angle / °
Cl04	Mn01	Cl02	112.878(14)
O006	Mn01	Cl02	109.55(3)
O006	Mn01	Cl04	108.04(3)
O007	Mn01	Cl02	110.13(3)
O007	Mn01	Cl04	113.79(3)
O007	Mn01	O006	101.80(4)
O006	P003	C008	110.80(6)
O006	P003	C009	110.95(5)
O006	P003	C00A	111.29(6)
C009	P003	C008	106.01(6)
C00A	P003	C008	108.59(6)
C00A	P003	C009	109.03(6)
O007	P005	C00B	110.73(6)
O007	P005	C00G	111.86(6)
O007	P005	C00N	110.92(6)
C00B	P005	C00G	108.23(6)
C00B	P005	C00N	108.40(6)
C00G	P005	C00N	106.53(6)
P003	O006	Mn01	155.54(6)
P005	O007	Mn01	163.62(7)
C00E	C008	P003	120.92(10)
C00E	C008	C00H	119.25(12)
C00H	C008	P003	119.82(10)
C00F	C009	P003	122.80(9)
C00F	C009	C00X	119.36(12)
C00X	C009	P003	117.75(10)
C00C	C00A	P003	122.40(9)
C00D	C00A	P003	118.07(10)
C00D	C00A	C00C	119.48(11)
C00J	C00B	P005	122.00(11)
C00J	C00B	C00Q	119.78(13)
C00Q	C00B	P005	118.21(11)
C00V	C00C	C00A	120.18(12)
C00K	C00D	C00A	119.79(12)
C00S	C00E	C008	120.59(12)
C00U	C00F	C009	119.81(12)
C00T	C00G	P005	118.05(10)
C015	C00G	P005	122.46(10)
C015	C00G	C00T	119.50(13)
C00P	C00H	C008	119.75(12)
C00K	C00I	C00V	120.38(12)
C00Z	C00J	C00B	119.66(14)

C00I	C00K	C00D	120.32(12)
C00O	C00L	C00N	120.03(13)
C010	C00M	C00N	119.69(13)
C00L	C00N	P005	121.12(10)
C00L	C00N	C00M	119.73(12)
C00M	C00N	P005	119.15(10)
C00Y	C00O	C00L	120.02(13)
C00W	C00P	C00H	120.56(13)
C011	C00Q	C00B	119.80(15)
C00U	C00R	C013	119.95(13)
C00W	C00S	C00E	119.90(13)
C012	C00T	C00G	119.99(14)
C00R	C00U	C00F	120.53(13)
C00C	C00V	C00I	119.83(13)
C00P	C00W	C00S	119.93(13)
C013	C00X	C009	120.16(13)
C010	C00Y	C00O	120.37(14)
C014	C00Z	C00J	120.11(15)
C00Y	C010	C00M	120.15(14)
C014	C011	C00Q	120.23(15)
C00T	C012	C017	120.10(15)
C00R	C013	C00X	120.17(13)
C011	C014	C00Z	120.41(14)
C00G	C015	C016	120.11(14)
C017	C016	C015	120.05(15)
C016	C017	C012	120.24(14)

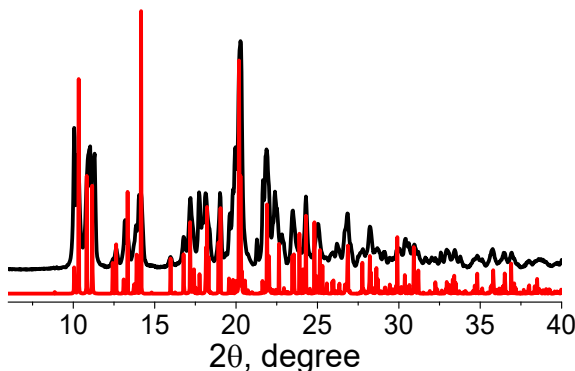


Fig. S1. Comparison of experimental (black) PXRD patterns of **1** with the diffraction pattern, simulated for the crystal structure (red).

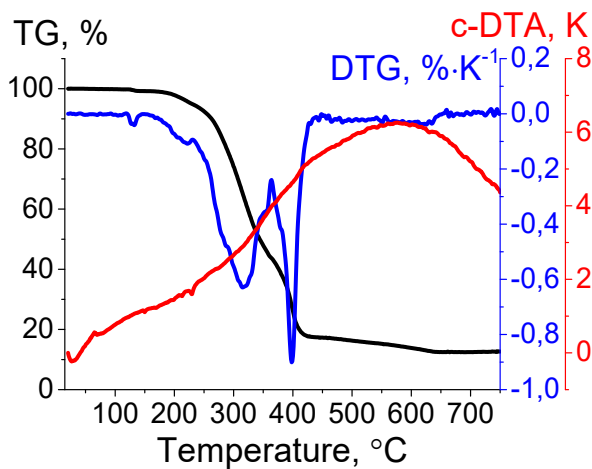


Fig. S2. TG, DTG, and c-DTA curves of **1**.

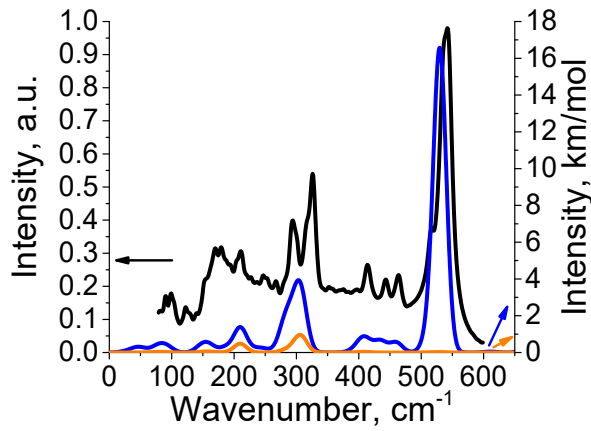


Fig. S3. Experimental (black) IR spectra of **1** with the calculated IR vibrations (blue) for the $[(\text{Ph}_3\text{PO})_2\text{MnCl}_2]$ molecule and partial contribution of the $\{\text{MnCl}_2\text{O}_2\}$ vibrations (orange).

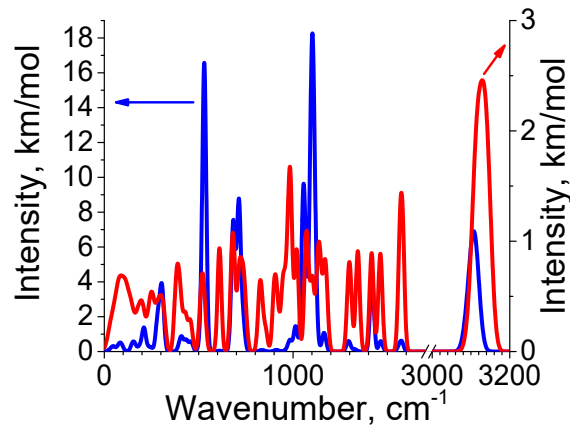


Fig. S4. Calculated IR vibrations for the $[(\text{Ph}_3\text{PO})_2\text{MnCl}_2]$ molecule (blue) and phonons for the $[(\text{Ph}_3\text{PO})_2\text{MnCl}_2]$ crystal (red).

Table S5. Calculated zero-field splitting parameters of **1**.

1DFT	
D_{tot} [MHz]	5403
E_{tot} [MHz]	1492
D_{SS} [MHz]	-752
E_{SS} [MHz]	-148
D_{SO} [MHz]	5384
E_{SO} [MHz]	1551
$D_{\alpha \rightarrow \beta}$ [MHz]	-2493
$E_{\alpha \rightarrow \beta}$ [MHz]	-861
$D_{\alpha \rightarrow \alpha}$ [MHz] ($D_{\alpha \rightarrow \alpha} / D_{\alpha \rightarrow \beta}$)	1009 (-0.40)
$E_{\alpha \rightarrow \alpha}$ [MHz] ($E_{\alpha \rightarrow \alpha} / E_{\alpha \rightarrow \beta}$)	252 (-0.30)

$$D_{\beta \rightarrow \beta} [\text{MHz}] (D_{\beta \rightarrow \beta} / D_{\alpha \rightarrow \beta}) \quad 2258 (-0.91)$$

$$E_{\beta \rightarrow \beta} [\text{MHz}] (E_{\beta \rightarrow \beta} / E_{\alpha \rightarrow \beta}) \quad 736 (-0.85)$$

$$D_{\beta \rightarrow \alpha} [\text{MHz}] (D_{\beta \rightarrow \alpha} / D_{\alpha \rightarrow \beta}) \quad 481 (-0.19)$$

$$E_{\beta \rightarrow \alpha} [\text{MHz}] (E_{\beta \rightarrow \alpha} / E_{\alpha \rightarrow \beta}) \quad 89 (-0.10)$$

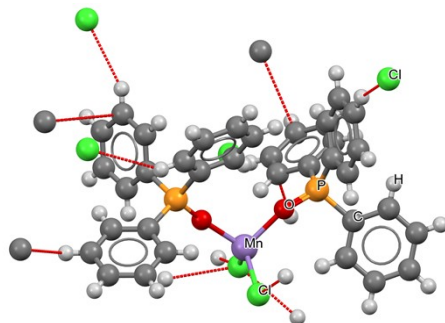
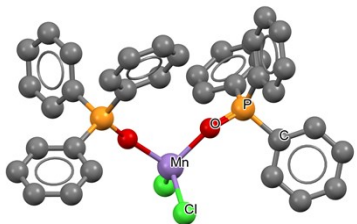


Fig. S5. Molecule structure of **1**. Molecule with omitted hydrogen for clarity (left) and molecule with shown short contacts by dotted red lines (right).

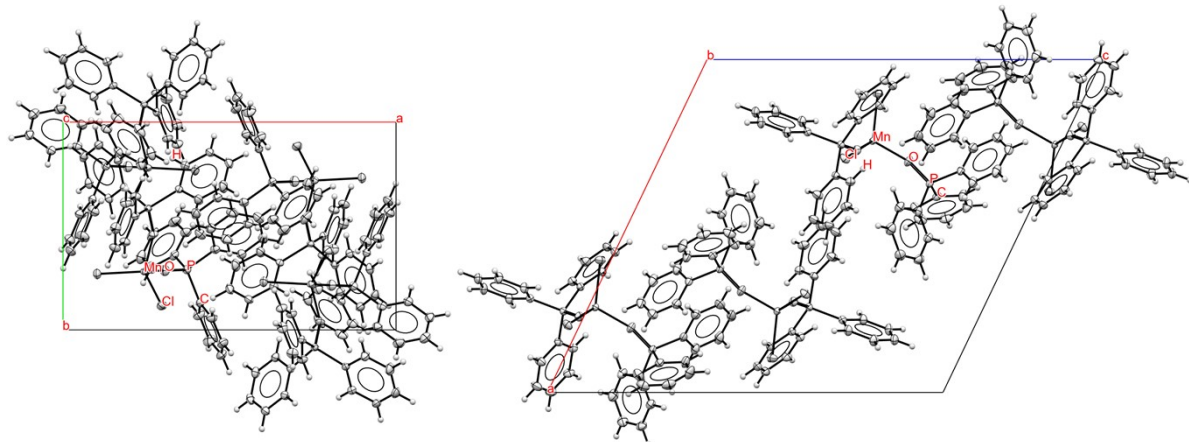


Fig. S6. ORTEP diagram of **1** crystal structure along axis **c** (left) and axis **b** (right).

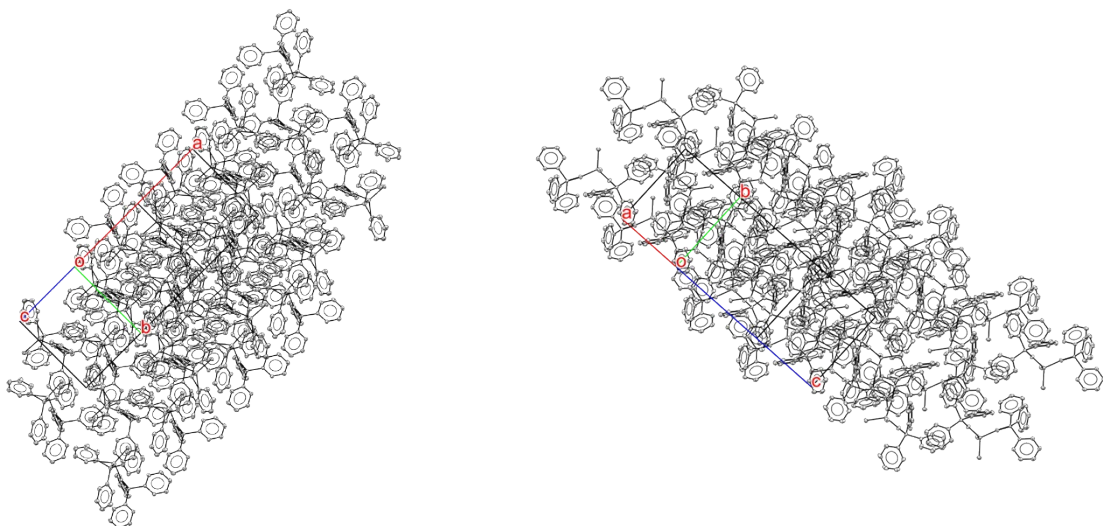


Fig. S7. ORTEP diagram of **1** crystal structure along (001) (left) and (100) (right) directions. Hydrogen atoms are omitted.

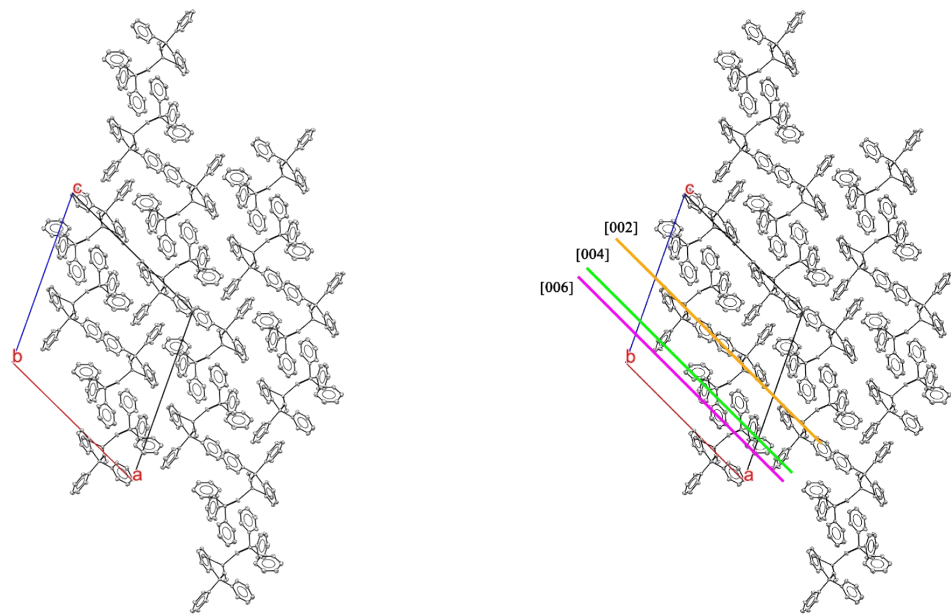


Fig. S8. ORTEP diagram of **1** crystal structure along (010) direction (left) with the selected [002], [004], and [006] planes (right). Hydrogen atoms are omitted.

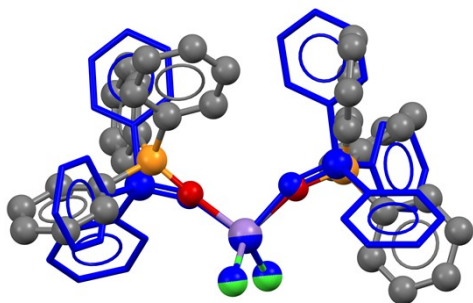


Fig. S9. Comparison of the molecule structures of **1** ($P2_1/n$, ball-and-stick, colored) and **1nl** ($Fdd2$, ball-and-stick and capped, blue) by overlaying the two Cl atoms and Mn atom.

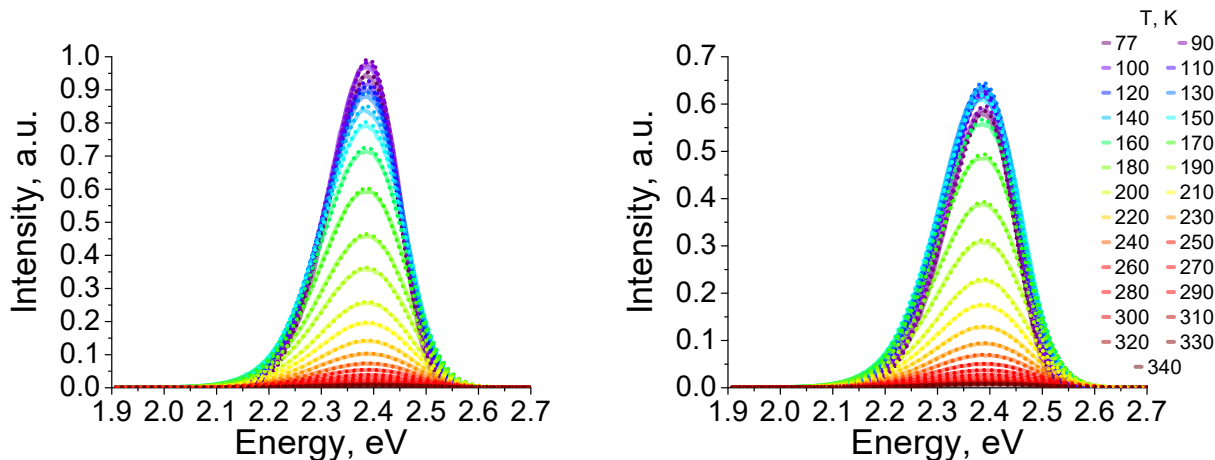


Fig. S10. Temperature dependence of the photoluminescence spectra ($\lambda_{\text{Ex}} = 275 \text{ nm}$ (left) and $\lambda_{\text{Ex}} = 280 \text{ nm}$ (right)) of **1**. Experimental (solid), two Gauss fitting (dot). Adjusted R^2 values for global parameters fitting are 0.999. Adjusted R^2 values for individual parameters fitting are 0.999 for temperatures 77 K – 270 K, 0.998 for temperatures 280 K – 290 K, and 0.997 for temperatures 300 K – 340 K.

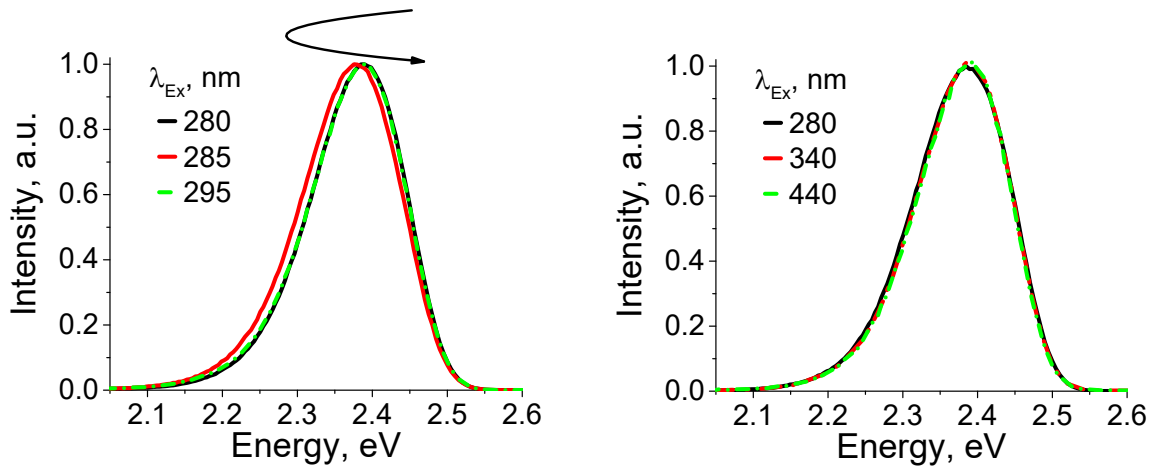


Fig. S11. Normalized photoluminescence spectra ($\lambda_{\text{Ex}} = 280 \text{ nm}$ (black), $\lambda_{\text{Ex}} = 285 \text{ nm}$ (red), and $\lambda_{\text{Ex}} = 295 \text{ nm}$ (green)) (left) and ($\lambda_{\text{Ex}} = 280 \text{ nm}$ (black), $\lambda_{\text{Ex}} = 340 \text{ nm}$ (red), and $\lambda_{\text{Ex}} = 440 \text{ nm}$ (green)) (right) of **1** at 77 K.

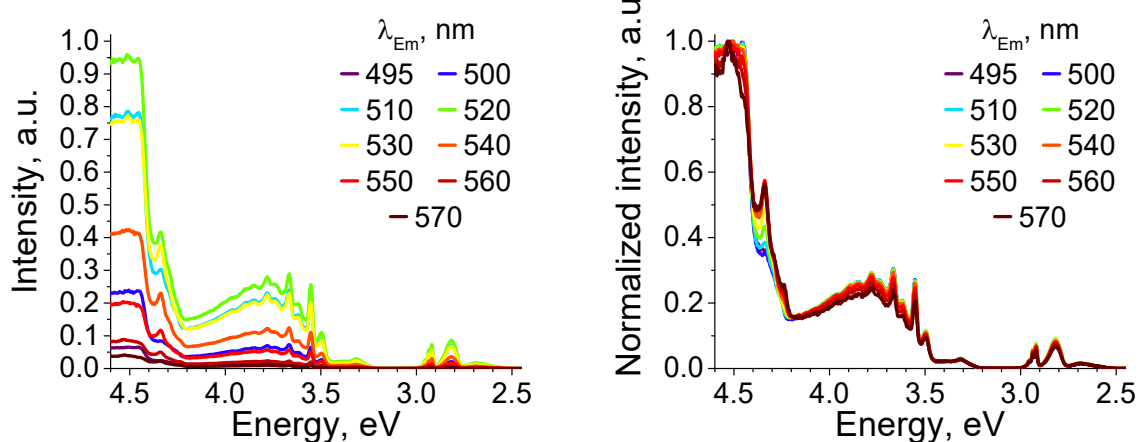


Fig. S12. Luminescence excitation spectra (left) and normalized (right) of **1** at 77 K.

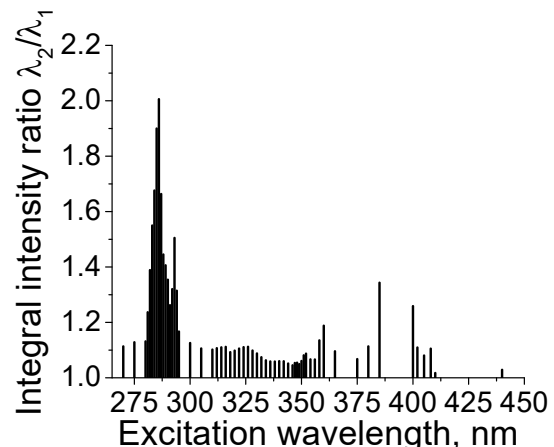


Fig. S13. Wavelength-excitation dependence of the integral intensity ratio λ_2/λ_1 ($\lambda_1 = 2.41 \text{ eV}$, $\lambda_2 = 2.35 \text{ eV}$) of the two Gauss fitted photoluminescence spectra of **1** at 77 K.

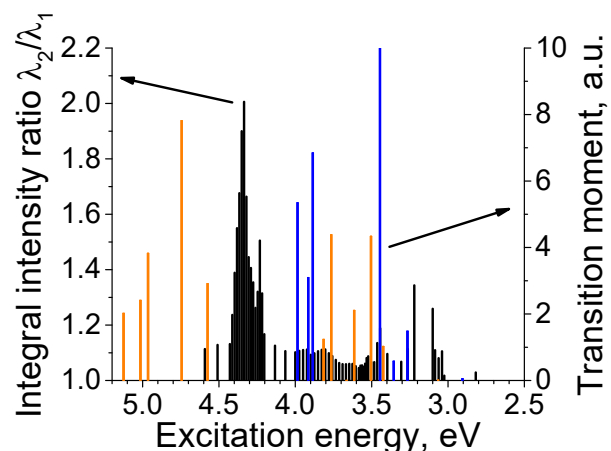


Fig. S14. Comparison of the wavelength-excitation dependence of the integral intensity ratio λ_2/λ_1 of **1** (black) at 77 K and calculated spin-flip transition energies for dimer $\{(\text{Ph}_3\text{PO})_2\text{MnCl}_2\}_2$ with C_i symmetry (orange – metal-and-halide to metal transition, blue - metal-and-halide to ligand transition).

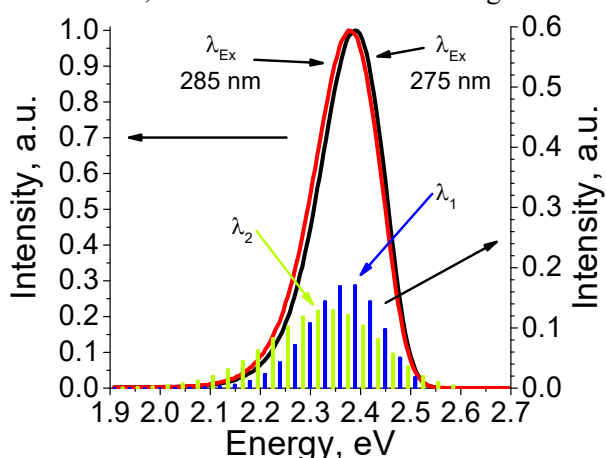


Fig. S15. Comparison of the experimental luminescence spectra of **1** ($\lambda_{\text{Ex}} = 275 \text{ nm}$ (black) and $\lambda_{\text{Ex}} = 285 \text{ nm}$ (red)) at 77 K with the reconstructed luminescence bands (λ_1 band (blue) and λ_2 band (green)). The reconstruction of the luminescence bands were carried out according to [35].

The energy dependence of the emission band intensity can be approximated by the following expression:

$$I = \frac{e^{-S} S^p}{p!} \left(1 + S^2 \frac{e^{-E_p/kT}}{p+1} \right), \quad p = \frac{E_0 - E}{E_p}$$

where E_0 is the zero phonon line energy, E_p is the phonon energy, S is the Huang–Rhys factor. The $E_p \approx 30 \text{ meV}$, $S_1 \approx 6$, and $E_0 \approx 2.54 \text{ eV}$ values were chosen for the λ_1 band and $E_p \approx 30 \text{ meV}$, $S_1 \approx 13$, and $E_0 \approx 2.71 \text{ eV}$ values were chosen for the λ_2 band.

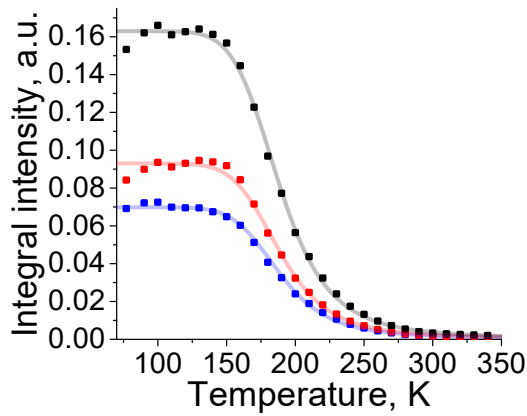


Fig. S16. Temperature dependences of the integral intensities ($\lambda_1 = 2.41$ eV (blue), $\lambda_2 = 2.35$ eV (red), and $\lambda_1 + \lambda_2$ (black)) of the two Gauss fitted (dot) photoluminescence spectra ($\lambda_{\text{Ex}} = 275$ nm) of **1**. Approximation (solid) by the equation $I(T) = I_0 / (1 + C * \exp\left(-\frac{\Delta E}{T}\right))$ (where I_0 is the intensity at $T = 0$ K, C is the dimensionless parameter corresponding to the ratio between the non-radiative and radiative probabilities, and ΔE is the activation energy for the thermal quenching process which is equal to the $\Delta E = 1970$ K (1370 cm^{-1})).

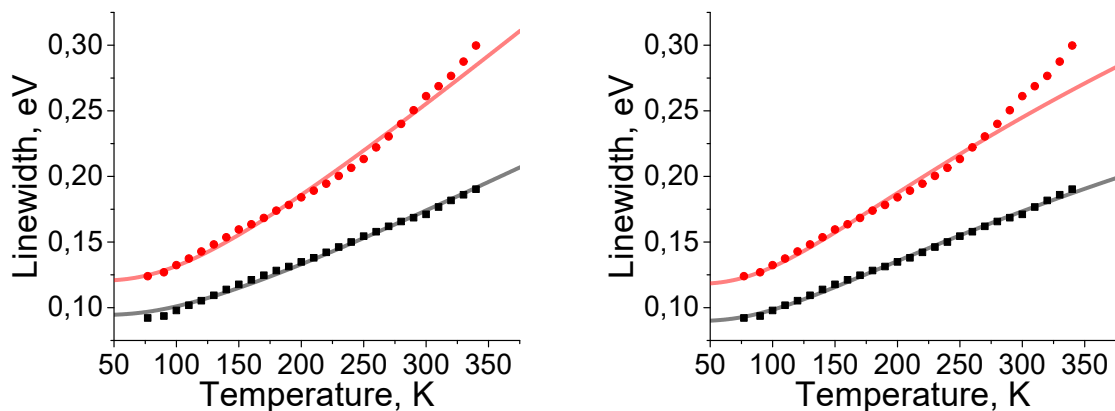


Fig. S17. Temperature dependences of the linewidth of the components of the photoluminescence spectrum of **1** ($\lambda_1 = 2.41$ eV (black) and $\lambda_2 = 2.35$ eV (red)) fitted by $w = \Gamma_0 + \Gamma_1 * (\exp\left(\frac{E_p}{k_B * T}\right) - 1)^{-1}$ (left) and by $w = 2 * \sqrt{S * E_p} * \sqrt[4]{\coth\left(\frac{E_p}{2 * k_B * T}\right) + w_0}$ (right). More details see in the article.

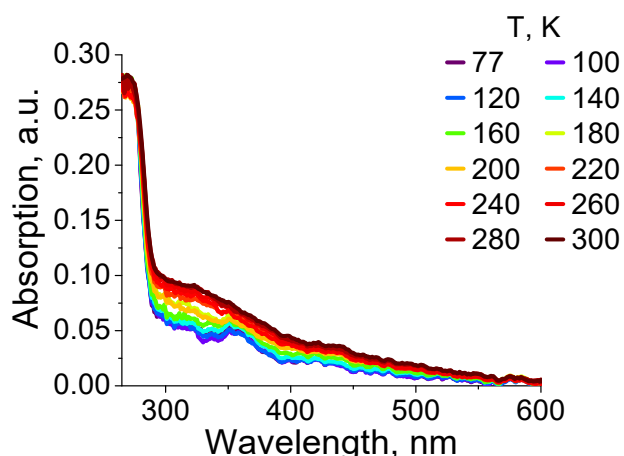


Fig. S18. Temperature dependence of the absorption of **1**.

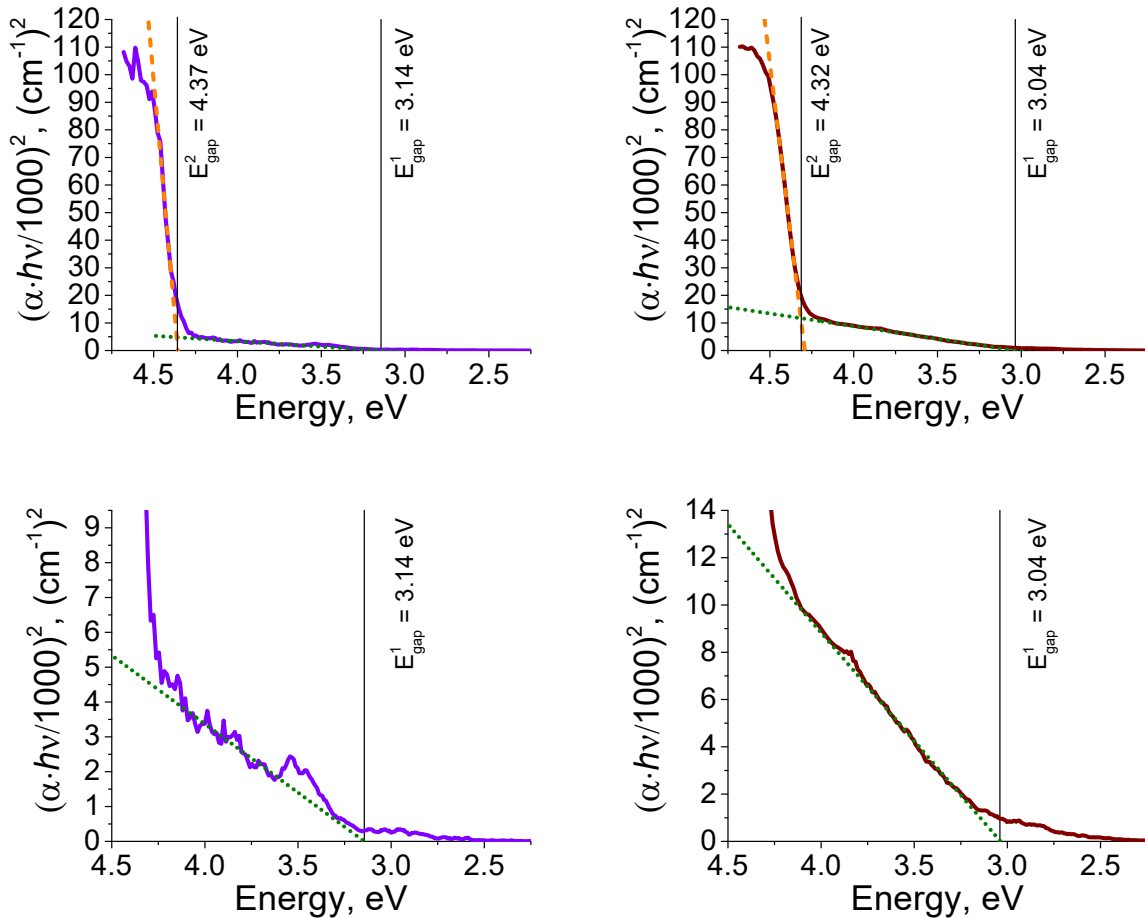


Fig. S19. Tauc plots for **1** at 77 K (left) and 300 K (right).

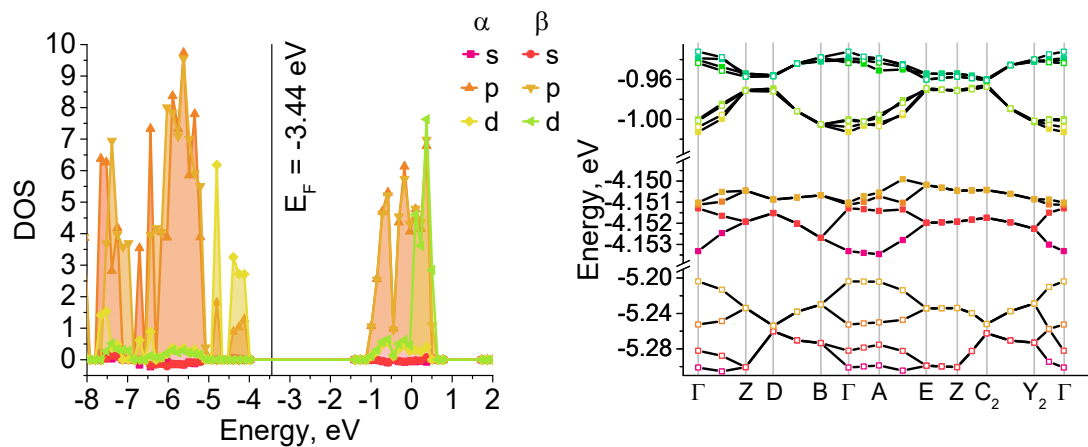


Fig. S20. Calculated DOS (left) and bandpaths (right) (spin-up (■) and spin-down (□)) for **1**.

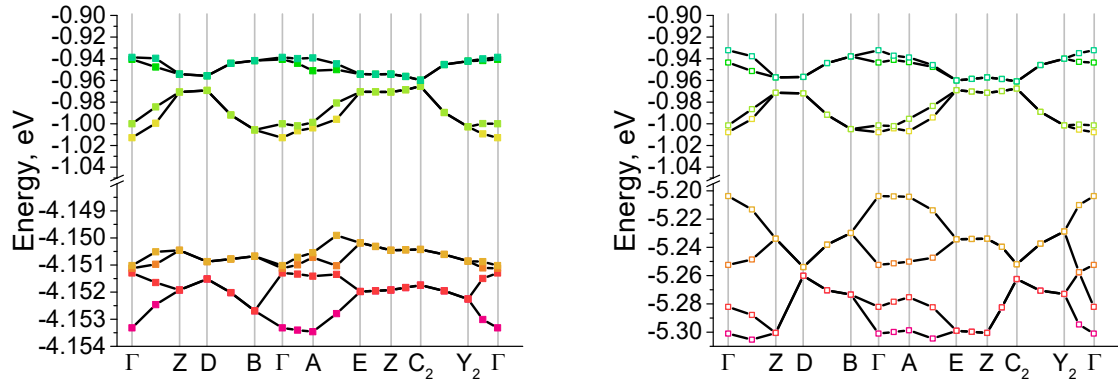


Fig. S21. Calculated spin-up (left) and spin-down (right) bandpaths for **1**.



Fig. S22. Photographs of single-crystal of **1** under cross-polarized light illumination at different angle between polarizes (0° , 30° , 60° , 90°)

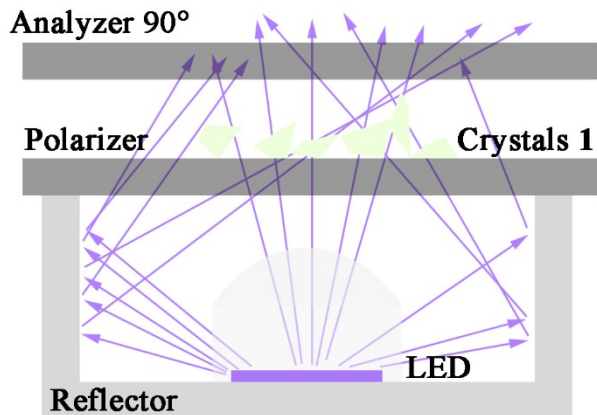


Fig. S23. Scheme of the fabricated LED with **1** under polarized light.



Fig. S24. Photographs of powder **1** under cross-polarized light illumination with 0° (left) and 90° (right) angle between polarizes. The LED with $\lambda_{\max} = 395\text{-}400\text{ nm}$ was used at 30 mW power.

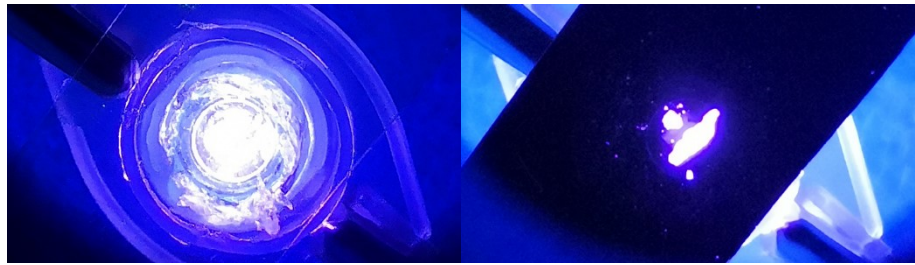


Fig. S25. Photographs of powder **1** under cross-polarized light illumination with 0° (left) and 90° (right) angle between polarizers. The LED with $\lambda_{\max} = 395\text{-}400 \text{ nm}$ was used at 90 mW power.

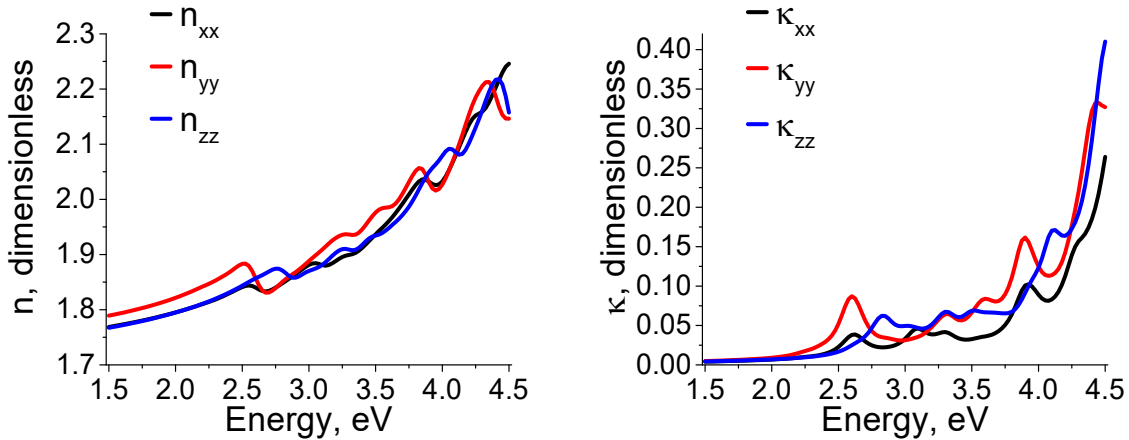


Fig. S26. Calculated energy dependence of the refractive tensor $n = n + i * \kappa$ of the $\{\text{(Ph}_3\text{PO)}_2\text{ZnCl}_2\}$ obtained from the energy dependence of the polarizability tensor α using the Lorentz-Lorenz equation $\frac{n^2 - 1}{n^2 + 2} = \frac{4\pi Z}{3 V} \alpha$, where Z is a number of molecule in the unit cell, V is a unit cell volume.

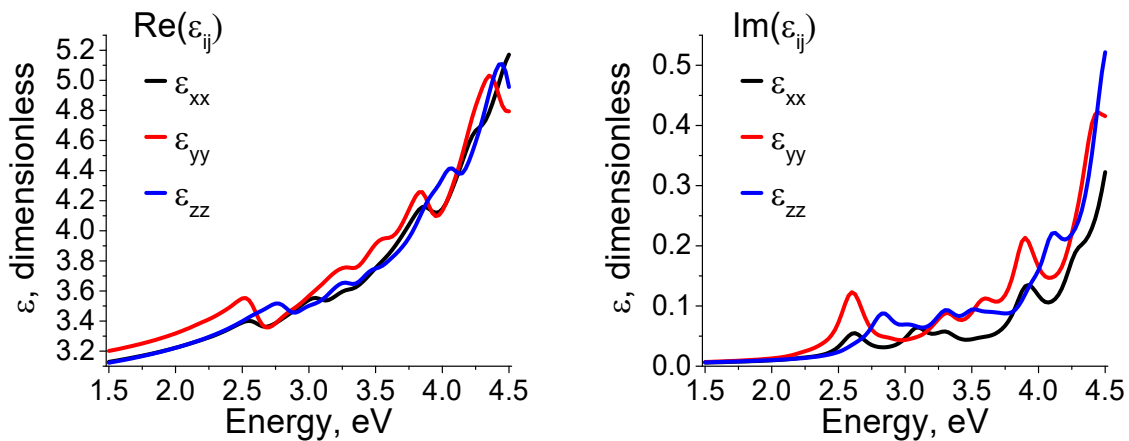


Fig. S27. Calculated energy dependence of the relative permittivity $\epsilon = \text{Re}(\epsilon) + i * \text{Im}(\epsilon)$ of the $\{\text{(Ph}_3\text{PO)}_2\text{ZnCl}_2\}$ obtained from the energy dependence of the polarizability tensor. ($\text{Re}(\epsilon) = n^2 - \kappa^2$, $\text{Im}(\epsilon) = 2 * n * \kappa$).

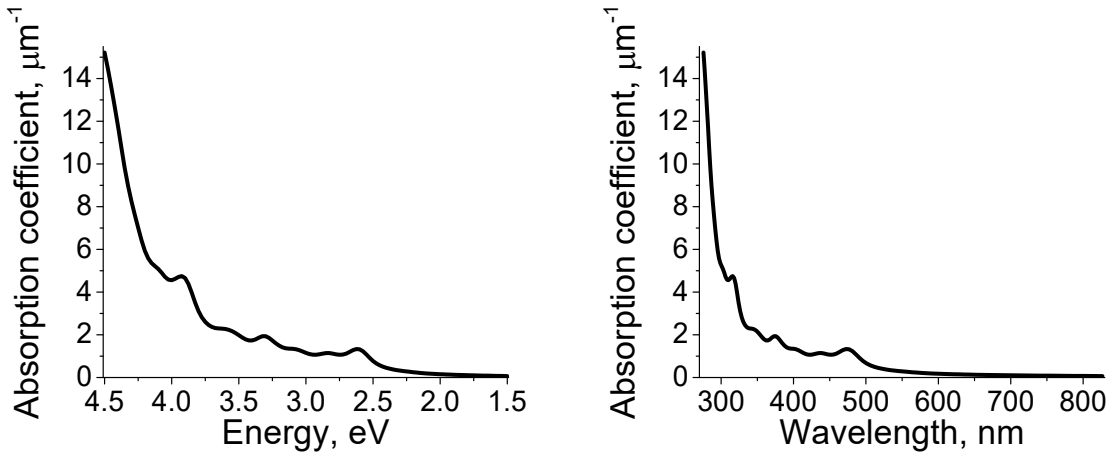


Fig. S28. Calculated energy dependence of the absorption coefficient $\text{absorption}(\lambda) = 4 * \pi * <\kappa(\lambda)>_{ij} / \lambda$, where $<\kappa(\lambda)>_{ij}$ is a spatially averaged absorption coefficient at wavelength λ of the $\{(Ph_3PO)_2ZnCl_2\}$.

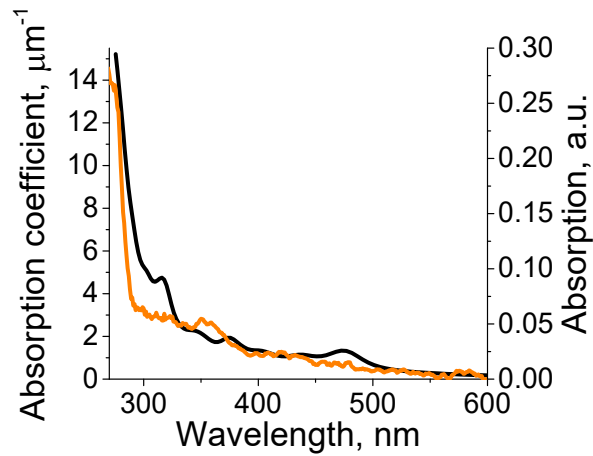


Fig. S29. Comparison of the absorption (black - calculated coefficient of the $\{(Ph_3PO)_2ZnCl_2\}$, orange - experimental absorption of **1** at 77 K).

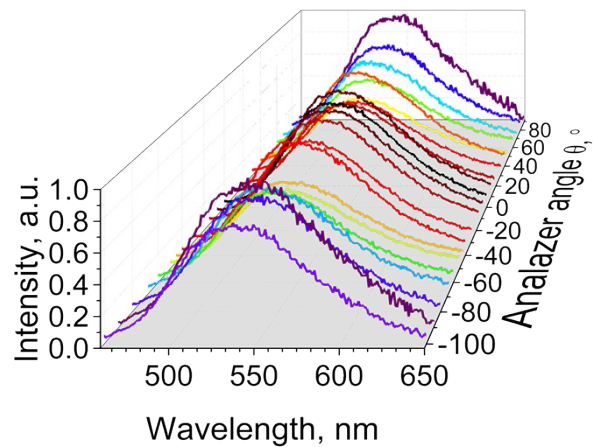


Fig. S30. Angular dependence of the polarized luminescence spectra of the single crystal **1**.

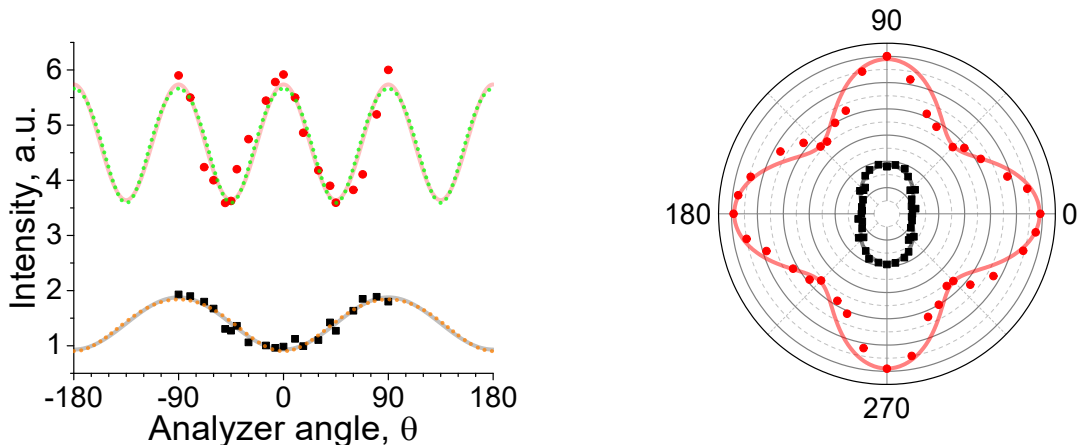


Fig. S31. Angular dependences of the integral intensities ($\lambda_{\text{Ex}} = 440 \text{ nm}$) of the λ_1 (black) and λ_2 (red) bands obtained from the two Gauss approximation of the polarized luminescence spectra of the single crystal **1** (at 300 K).

Comparison of the fitting by $I(\theta) = A * \cos^2(m * \theta + \varphi) + A_0$ (solid) and $I(\theta) = A * (3 * \cos^2(m * \theta + \varphi) - 1) / (\cos^2(m * \theta + \varphi) + 3) + A_0$ (dot). Adjusted R-Squared value of the two Gauss approximation fitting is 0.997. Adjusted R-Squared value of the angular dependence fitting is 0.955.

$$P_i = \frac{A_{\max} - A_{\min}}{A_{\max} + A_{\min}}$$

The experimental degree of polarization for λ_1 and λ_2 bands are $P_1 = 0.45$ and $P_2 = 0.25$ where

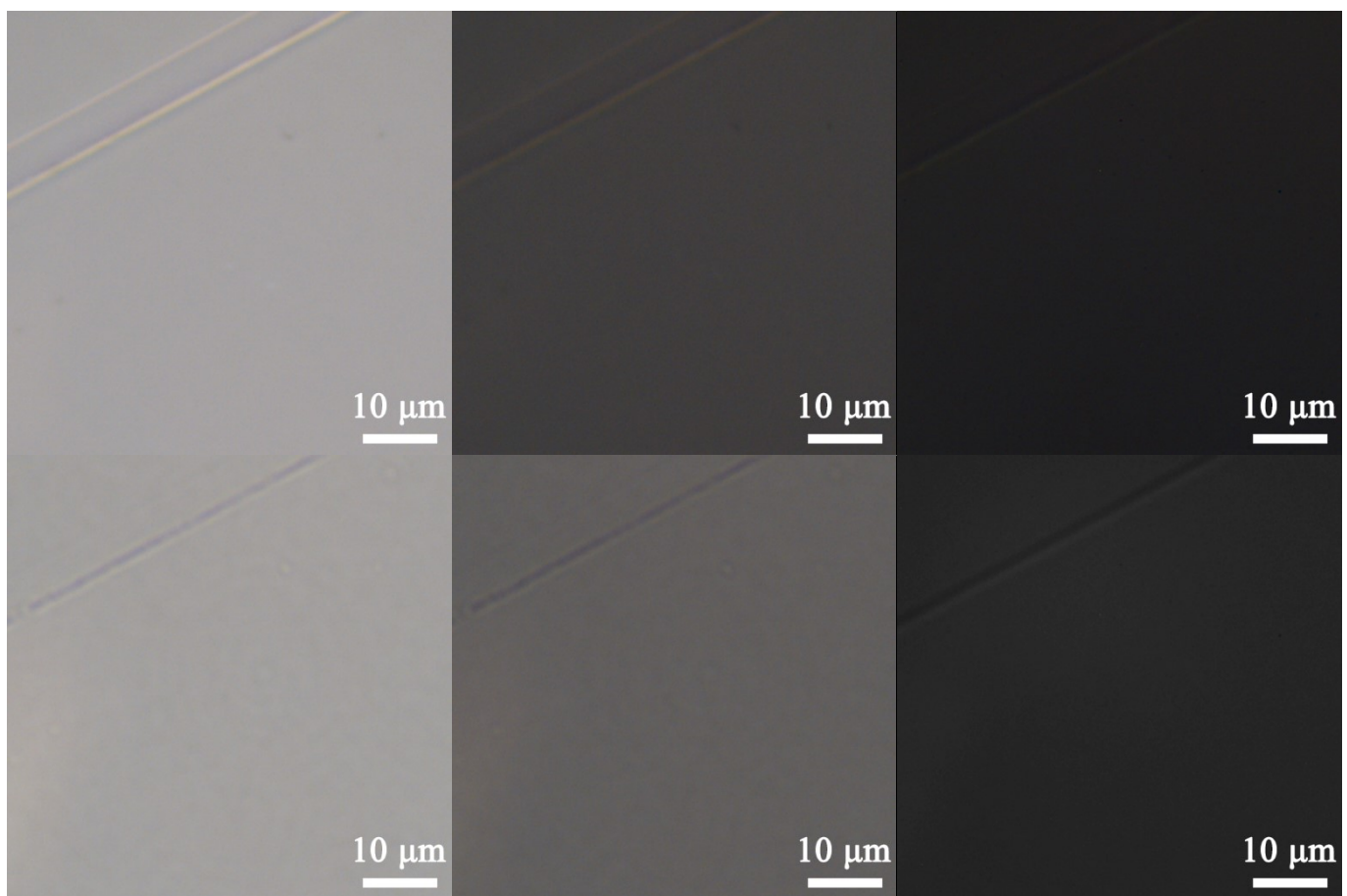


Fig. S32. Photographs of the film of **1** on the quartz substrate obtained by spin-coating method under white-light illumination (left), under cross-polarized white-light illumination at angle polarizes 0° (center) and 90° (right) in reflection mode (top) and in transmission mode (bottom).

The analysis of the film thickness h according to the absorption data and quantum chemical-calculations gives the value $h \sim 200 \text{ nm}$ in order of magnitude. The thickness is estimated using the formula $h = \text{absorption}(\lambda) * \lambda / 4 * \pi * <\kappa(\lambda)>_{ij}$, where $\text{absorption}(\lambda)$ is an experimentally obtained absorption value of

the film at wavelength λ , $\langle \kappa(\lambda) \rangle_{ij}$ is a spatially averaged absorption coefficient at wavelength λ obtained from quantum chemical-calculations.

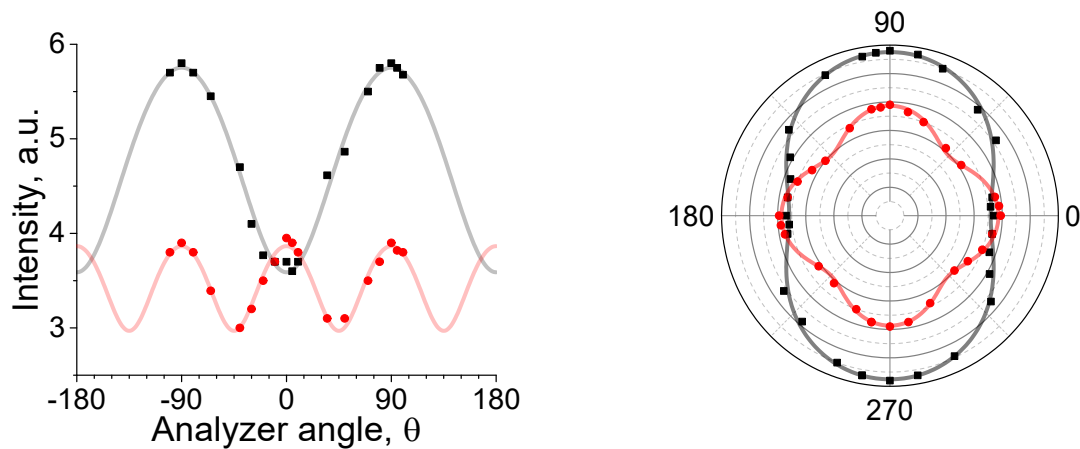


Fig. S33. Angular dependences of the integral intensities ($\lambda_{\text{Ex}} = 440$ nm) of the λ_1 (black) and λ_2 (red) bands obtained from the two Gauss approximation of the polarized luminescence spectra of the **1** coated on the glass substrate (at 300 K). Adjusted R-Squared value is 0.958.

$$P_i = \frac{A_{\max} - A_{\min}}{A_{\max} + A_{\min}}$$

The experimental degree of polarization for λ_1 and λ_2 bands are $P_1 = 0.24$ and $P_2 = 0.14$ where

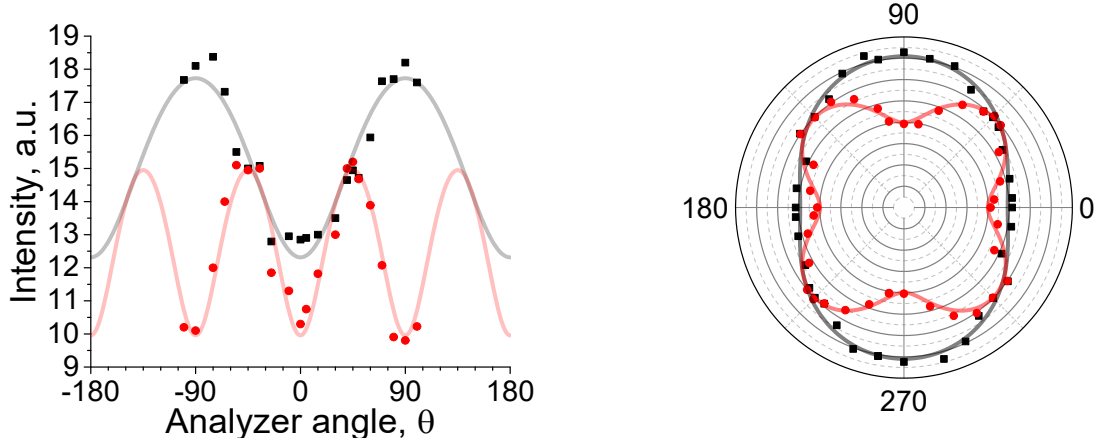


Fig. S34. Angular dependences of the integral intensities ($\lambda_{\text{Ex}} = 440$ nm) of the λ_1 (black) and λ_2 (red) bands obtained from the two Gauss approximation of the polarized luminescence spectra of the **1** coated on the glass substrate (at 77 K). Adjusted R-Squared value is 0.981.

$$P_i = \frac{A_{\max} - A_{\min}}{A_{\max} + A_{\min}}$$

The experimental degree of polarization for λ_1 and λ_2 bands are $P_1 = 0.18$ and $P_2 = 0.22$ where

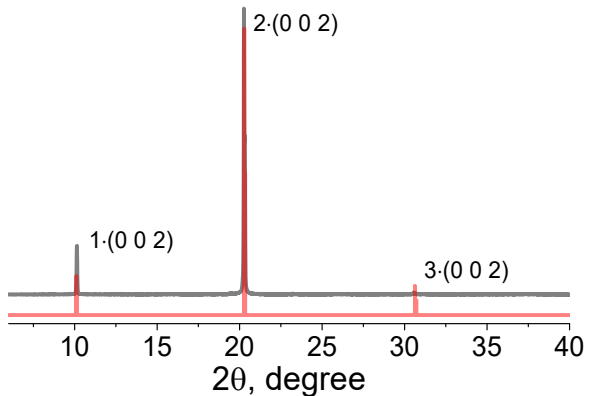


Fig. S35. Comparison of experimental (black) PXRD patterns of **1** with the diffraction pattern ((00 l) plane), simulated for the crystal structure (red).

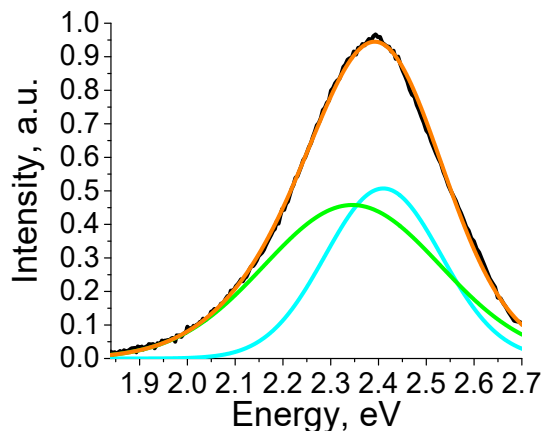


Fig. S36. Photoluminescence spectrum ($\lambda_{\text{Ex}} = 300$ nm) of the film of **1** on the quartz substrate obtained by spin-coating method. Experimental (black), two Gauss fitting with maxima $\lambda_1 = 2.41$ eV (cyan) and $\lambda_2 = 2.35$ eV (green), superposition of the two fitting Gauss functions (orange).

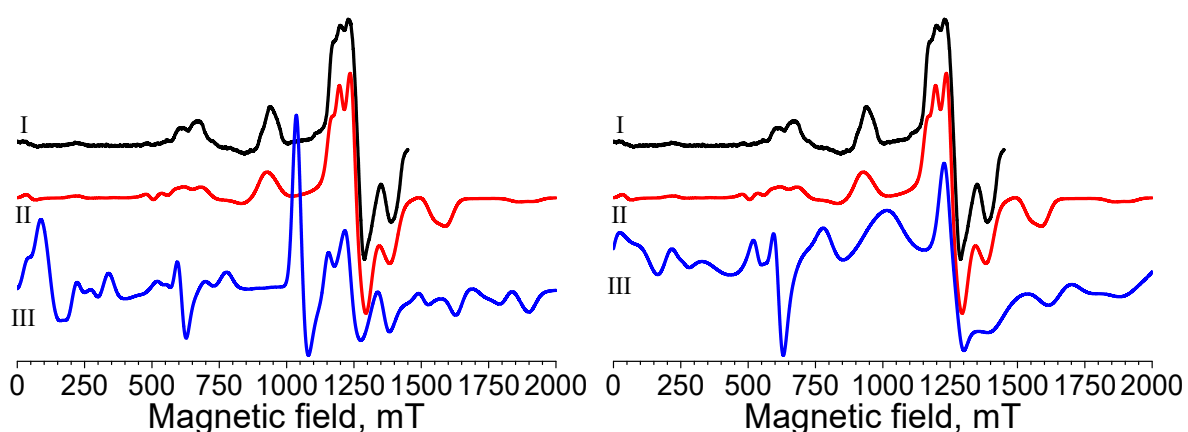


Fig. S37. Q-band powder EPR spectra at 300 K (black line – experimental for **1**, red line – the best fit of the experimental data of **1**, blue line –fitting of the literature data for **1nL** [36]) with the equal line width values for II and III (left) and with different line width values for II and III (right).

36 Dowsing, R. D., Gibson, J. F., Goodgame, D. M. L., Goodgame, M., Hayward, P. J., *Journal of the Chemical Society A: Inorganic, Physical, and Theoretical Chemistry* (1969), 1242, <http://doi.org/10.1039/J19690001242>.

Table S6. Fractional Atomic Coordinates ($\times 10^4$) for **1** after quantum-chemical calculation.

Atom	x	y	z
Mn	2433.8	2807.5	5140.8
Cl	2964.8	1101.3	4700.8
P	2538.9	5851.2	4387.5

Cl	1020.7	2669.7	4670.5
P	3710.9	2971.3	7099.6
O	2740.2	4622.4	4893.0
O	3009.7	2911.2	6294.1
C	2161.5	5399.9	3388.1
C	3447.8	6840.1	4614.4
C	1794.0	6864.1	4526.0
C	3355.2	3701.9	7750.8
C	1648.3	8174.4	4270.7
H	2004.0	8631.4	4003.4
C	1350.3	6301.8	4892.3
H	1457.1	5280.5	5080.8
C	2230.1	6274.9	2858.1
H	2522.7	7230.4	3045.4
C	3630.4	7915.5	5114.7
H	3192.2	8243.8	5324.8
C	4116.6	1361.6	7467.3
C	1798.2	4162.0	3145.4
H	1736.2	3484.3	3553.7
C	615.8	8351.5	4744.1
H	155.7	8922.6	4835.0
C	3763.3	4756.2	8232.8
H	4324.1	5148.9	8232.5
C	760.9	7049.9	4998.3
H	405.0	6621.9	5274.0
C	5352.8	3750.2	7738.1
H	5449.8	3031.8	8187.6
C	4448.8	4851.1	6556.8
H	3843.7	4966.3	6081.3
C	4571.4	3924.3	7132.5
C	6010.2	4506.3	7767.1
H	6616.0	4369.2	8239.6
C	1515.0	3800.5	2377.9
H	1233.3	2838.1	2192.6
C	2632.6	3194.3	7752.5
H	2309.2	2386.3	7370.6
C	4931.9	8191.1	5053.8
H	5511.3	8711.2	5222.1
C	1947.0	5907.2	2092.7
H	2014.4	6569.1	1681.3

Table S7. Calculated singlet-singlet and spin-flip transition energies for the $[(\text{Ph}_3\text{PO})_2\text{MnCl}_2]$ molecule of **1** (CAM-B3LYP, scalar ZORA).

№	Singlet-singlet transition			Spin-flip transition	
	Energy, eV	Wavelength, nm	Oscillator strength $f \cdot 10^{-6}$, a.u	Energy, eV	Wavelength, nm
1	3.9690	312.42	0.14	2.5034	495.32
2	3.9983	310.13	610.08	2.5402	488.15
3	4.0013	309.90	23.18	2.5920	478.40
4	4.0133	308.97	165.41	2.5989	477.12
5	4.0224	308.27	8.91	2.6075	475.55
6	4.0512	306.08	14.44	2.6247	472.43
7	4.3909	282.40	4133.28	2.6854	461.76
8	4.4286	280.00	62.26	2.7213	455.66
9	4.4564	278.25	120.29	2.7275	454.63
10	4.4823	276.64	20.70	2.7553	450.05
11	4.4889	276.24	91.92	2.7641	448.61
12	4.4986	275.64	10.93	2.7767	446.58
13	4.5324	273.58	102.94	2.8817	430.30

14	4.5523	272.39	3300.23	2.8993	427.69
15	4.5862	270.38	1093.06	3.6081	343.67
16	4.6555	266.35	12473.13	3.7061	334.58
17	4.6629	265.93	173.78	3.8467	322.36
18	4.6849	264.68	802.80	3.9253	315.90
19	4.6905	264.36	285.90	3.9351	315.11
20	4.6997	263.85	855.86	3.9681	312.49
21	4.7066	263.46	124.41	3.9784	311.69
22	4.7252	262.42	5274.40	3.9893	310.83
23	4.7675	260.10	1328.99	3.9937	310.49
24	4.8567	255.32	16605.22	4.0062	309.52
25	4.8762	254.29	4134.04	4.0211	308.37

Table S8. Calculated spin-flip transition energies for the $\{[(\text{Ph}_3\text{PO})_2\text{MnCl}_2]\}_2$ dimer with C_i symmetry of **1** (CAM-B3LYP, scalar ZORA). The underlined transitions has a dominant contribution of the metal-and-halide to metal transition (d - d and XMCT).

№	Spin-flip transition	
	Energy, eV	Wavelength, nm
1	2.9148	425.42
2	<u>3.0590</u>	<u>405.36</u>
3	3.2662	379.65
4	3.3650	368.50
5	<u>3.4207</u>	<u>362.50</u>
6	3.4493	359.49
7	<u>3.4961</u>	<u>354.68</u>
8	<u>3.6098</u>	<u>343.51</u>
9	<u>3.6596</u>	<u>338.83</u>
10	<u>3.7645</u>	<u>329.39</u>
11	<u>3.8095</u>	<u>325.50</u>
12	3.8892	318.83
13	3.9180	316.49
14	3.9900	310.78
15	<u>4.5726</u>	<u>271.18</u>
16	<u>4.7406</u>	<u>261.57</u>
17	<u>4.9553</u>	<u>250.24</u>
18	<u>5.0110</u>	<u>247.46</u>
19	<u>5.1225</u>	<u>242.07</u>

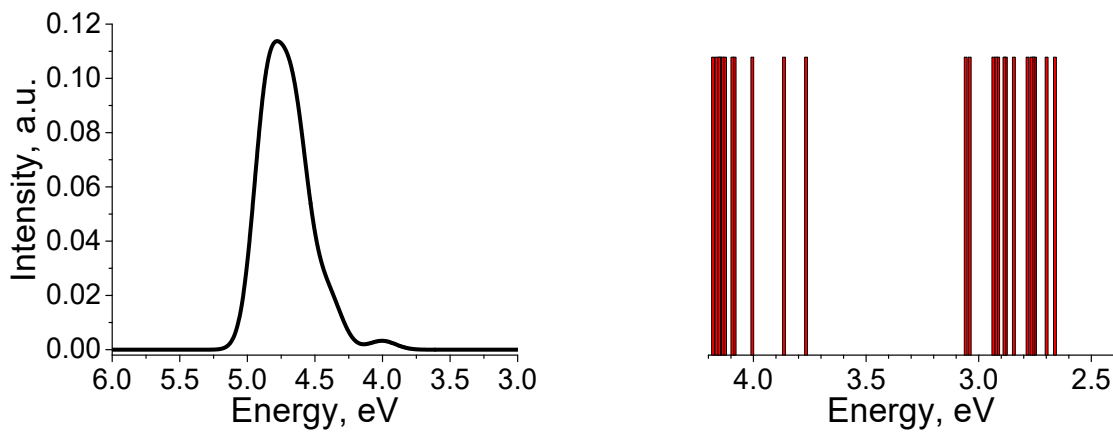


Fig. S38. Calculated UVVis transition spectrum with $w = 0.2$ eV (left) and spin-flip transition energies (right) of **1**.

Table S9. Calculated singlet-singlet and singlet-triplet transition energies for the two different $\{\text{Ph}_3\text{PO}\}$ fragments of $[(\text{Ph}_3\text{PO})_2\text{MnCl}_2]$ molecule of **1** (CAM-B3LYP, scalar ZORA).

	First $\{\text{Ph}_3\text{PO}\}$ fragment	Second $\{\text{Ph}_3\text{PO}\}$ fragment
--	---	--

	Singlet-singlet transition		Singlet-triplet transition	Singlet-singlet transition		Singlet-triplet transition
Nº	Energy, eV	Oscillator strength $f \cdot 10^{-3}$, a.u	Energy, eV	Energy, eV	Oscillator strength $f \cdot 10^{-3}$, a.u	Energy, eV
1	5.2913	3.27	3.9637	5.3148	4.03	3.9828
2	5.3124	7.48	3.9708	5.3454	5.52	4.0002
3	5.3568	14.52	4.0463	5.3601	3.78	4.0214
4	5.5610	10.84	4.5373	5.4696	84.48	4.5687
5	5.5862	81.75	4.5600	5.6798	28.10	4.5874
6	5.7268	17.90	4.5658	5.8205	20.05	4.6012
7	5.8655	197.04	4.6763	5.9087	1.92	4.6833
8	5.9022	40.00	4.6821	6.0135	50.50	4.6939
9	6.1468	52.47	4.7183	6.1658	50.50	4.7070
10	6.2835	1.63	5.1156	6.1729	41.76	5.1010
11	6.3241	30.39	5.1190	6.2813	17.19	5.1334
12	6.4401	74.48	5.1825	6.3029	8.81	5.1685
13	6.4956	22.62	5.3995	6.3812	56.22	5.3992
14	6.5342	2.90	5.4167	6.4798	12.85	5.5136
15	6.5429	4.78	5.6421	6.6169	42.01	5.6720
16	6.5868	6.56	5.7794	6.7038	120.51	5.7946
17	6.6034	1.41	6.1267	6.7224	64.89	5.9255
18	6.6452	41.77	6.2517	6.7661	16.37	6.1066
19	6.7241	272.65	6.4113	6.7864	13.56	6.3906
20	6.7720	86.88	6.4406	6.8002	74.04	6.4430
21	6.8386	124.89	6.5133	6.8392	241.39	6.5029
22	6.8621	119.88	6.5417	6.8735	25.21	6.6548
23	6.8724	10.31	6.5509	6.8755	6.88	6.6791
24	6.8919	179.71	6.6581	6.9229	14.07	6.6991
25	6.9535	51.31	6.7126	6.9492	42.85	6.7563

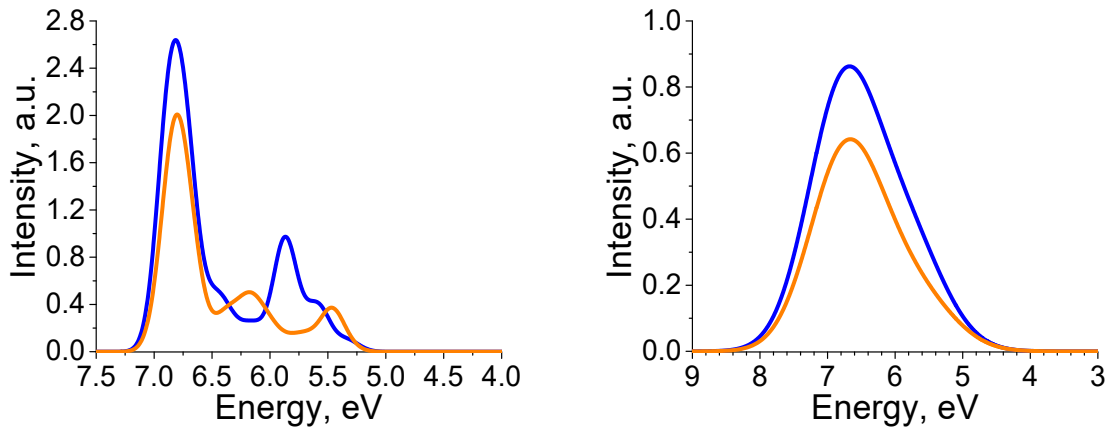


Fig. S39. Calculated UVVis transition spectra with $w = 0.2$ eV (left) and $w = 1.0$ eV (right) for the two different $\{\text{Ph}_3\text{PO}\}$ fragments of $[(\text{Ph}_3\text{PO})_2\text{MnCl}_2]$ molecule of 1.

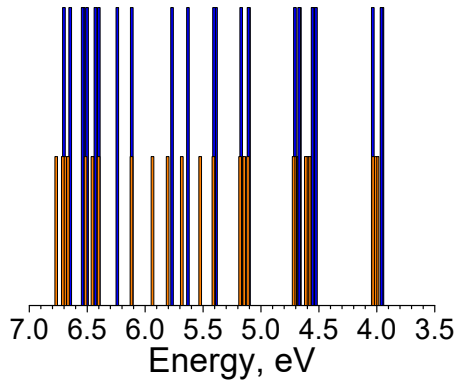


Fig. S40. Calculated spin-flip transition energies for the two different $\{\text{Ph}_3\text{PO}\}$ fragments of $[(\text{Ph}_3\text{PO})_2\text{MnCl}_2]$ molecule of **1**.

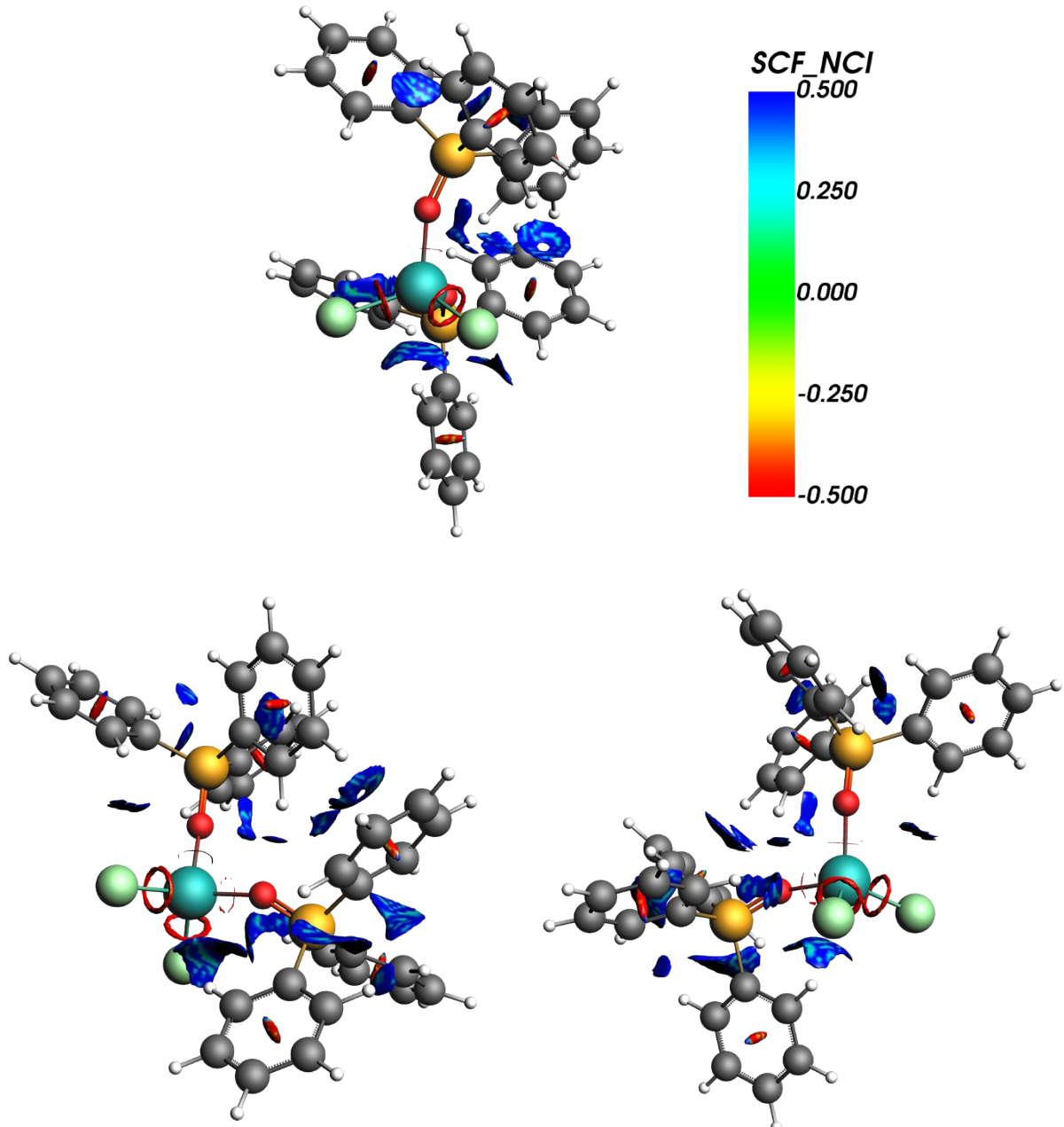


Fig. S41. The noncovalent interaction (NCI) plots for the $[(\text{Ph}_3\text{PO})_2\text{MnCl}_2]$ molecule of **1**. NCIs (SCF density) are presented by isosurfaces ($s = 0.5$ a.u., $\rho = 0.02$ a.u.) colored according to $\text{sign}(\lambda_2)\rho$ in the red-green-blue scheme.

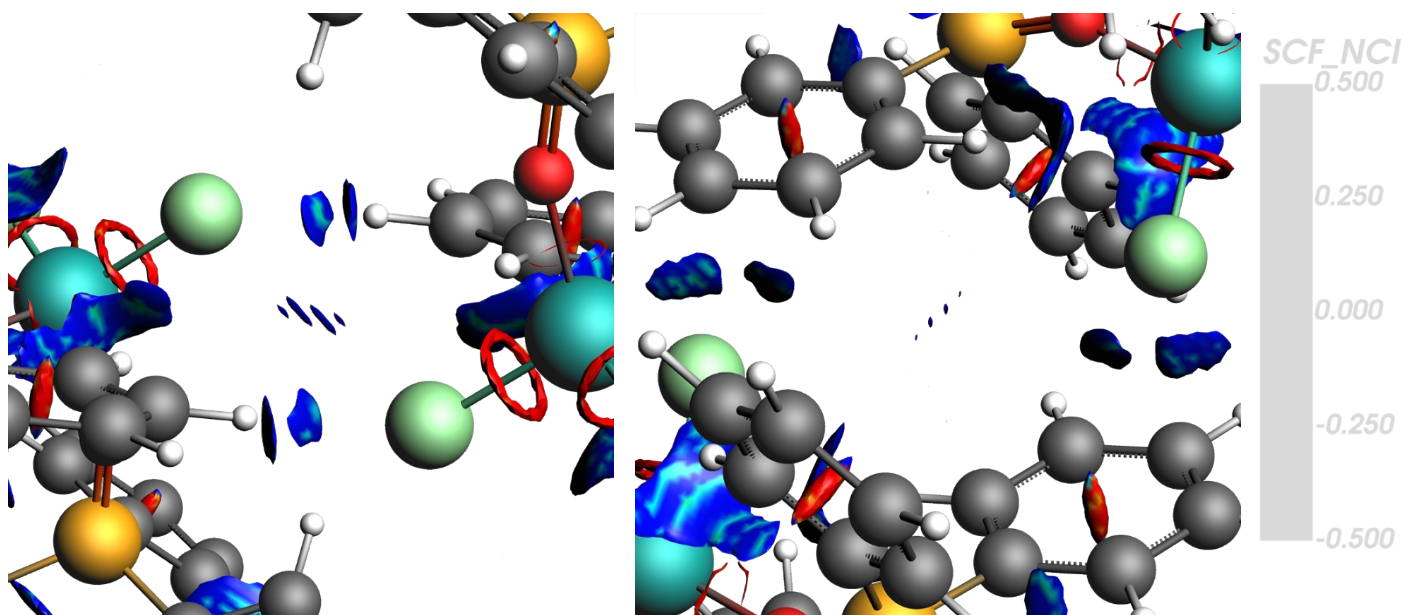


Fig. S42. The noncovalent interaction (NCI) plots for the $\{[(\text{Ph}_3\text{PO})_2\text{MnCl}_2]\}_2$ dimer (C_i symmetry) of **1**. NCI_s (SCF density) are presented by isosurfaces ($s = 0.5$ a.u., $\rho = 0.02$ a.u.) colored according to $\text{sign}(\lambda_2)\rho$ in the red-green-blue scheme.

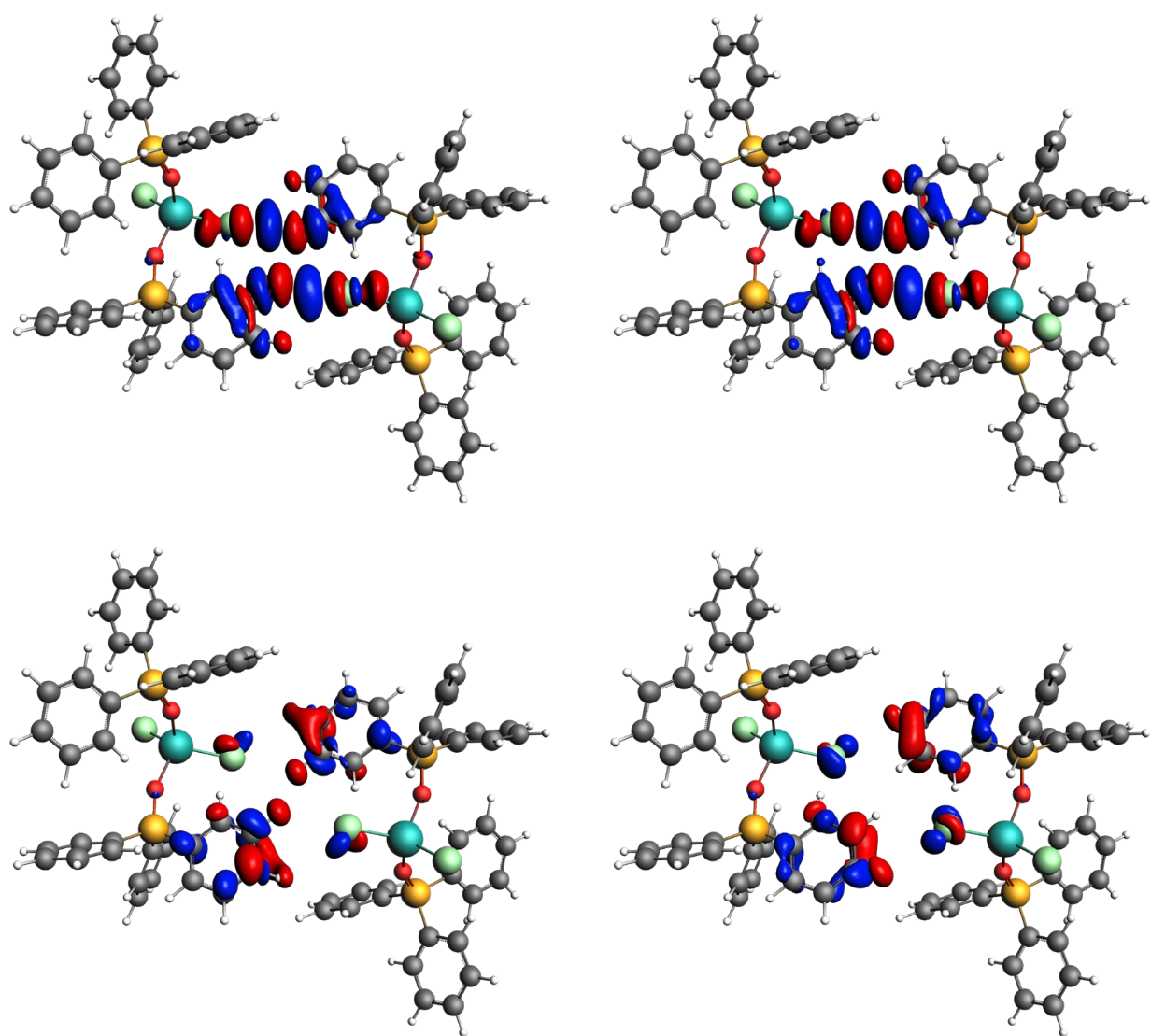


Fig. S43. The calculated deformation density $\Delta\rho_i$ (α -spin) for the $\{[(\text{Ph}_3\text{PO})_2\text{MnCl}_2]\}_2$ dimer (C_i symmetry) formation from the two monomers $[(\text{Ph}_3\text{PO})_2\text{MnCl}_2]$ of **1** with NOCV eigenvalues: left-top – $|V| = 0.0475$; right-top – $|V| = 0.0436$; left-bottom – $|V| = 0.0297$; right-bottom – $|V| = 0.0293$. Red for $\Delta\rho_i < 0$ and blue for $\Delta\rho_i > 0$.

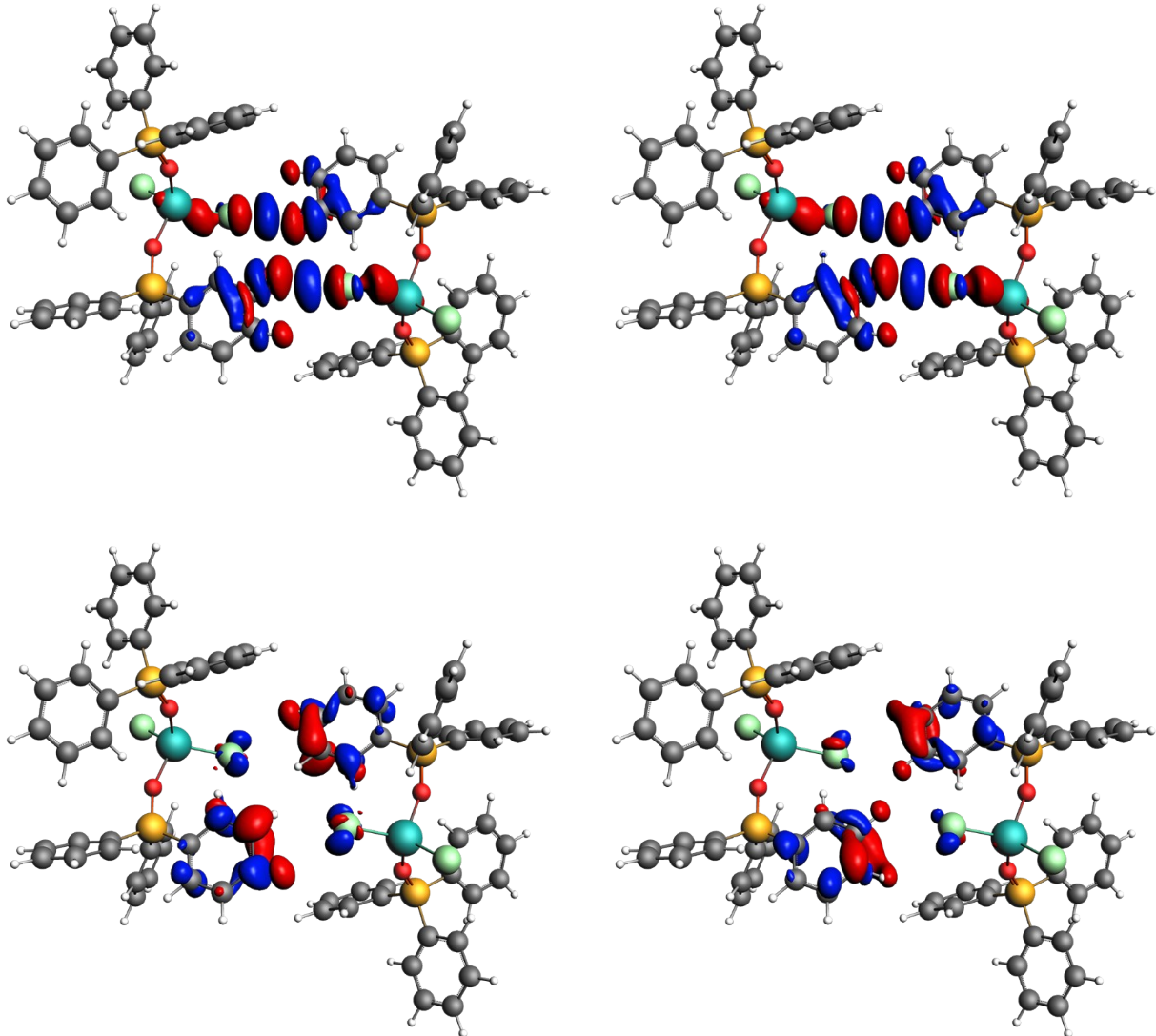
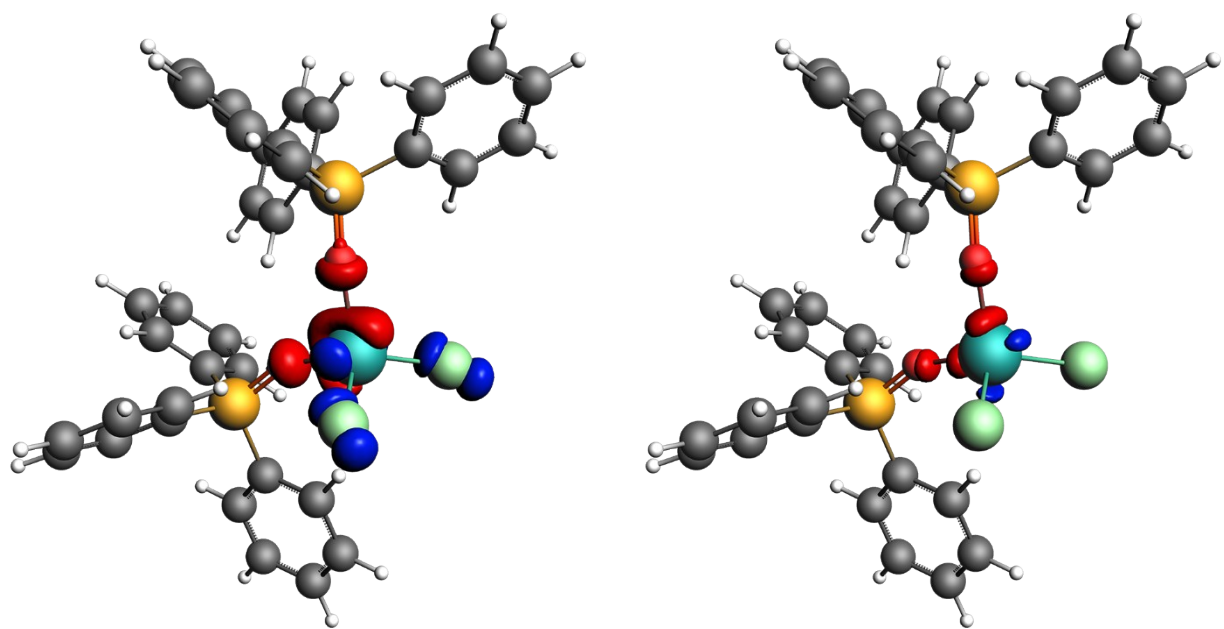


Fig. S44. The calculated deformation density $\Delta\rho_i$ (β -spin) for the $\{[(\text{Ph}_3\text{PO})_2\text{MnCl}_2]\}_2$ dimer (C_i symmetry) formation from the two monomers $[(\text{Ph}_3\text{PO})_2\text{MnCl}_2]$ of **1** with NOCV eigenvalues: left-top – $|V| = 0.0403$; right-top – $|V| = 0.0387$; left-bottom – $|V| = 0.0252$; right-bottom – $|V| = 0.0246$. Red for $\Delta\rho_i < 0$ and blue for $\Delta\rho_i > 0$.



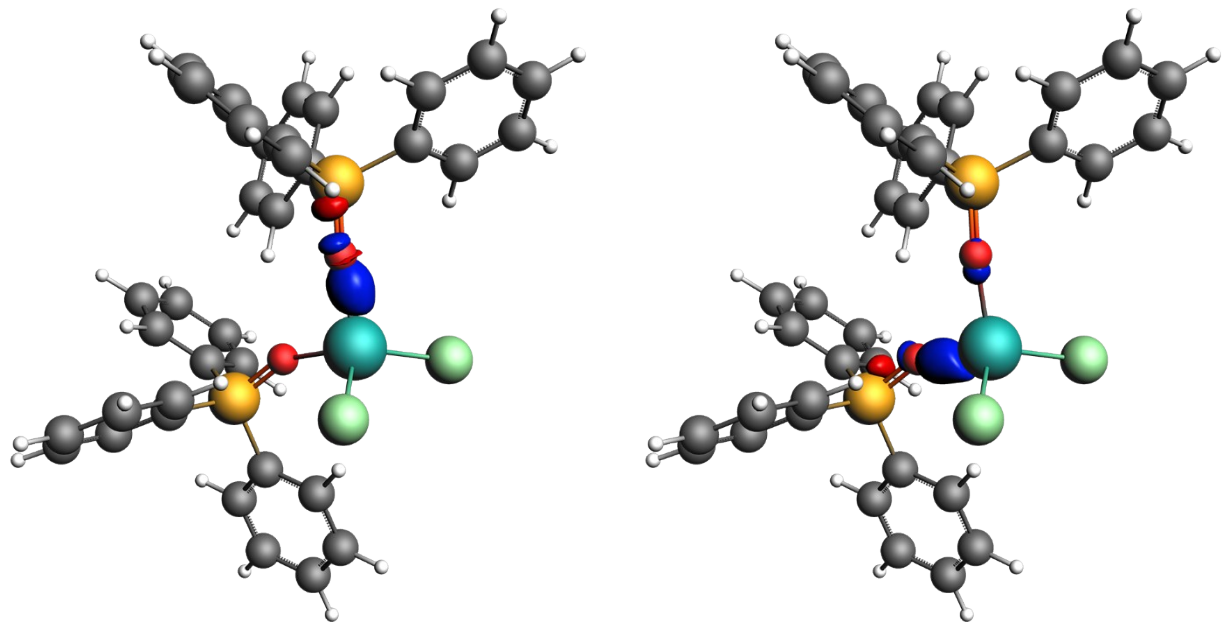
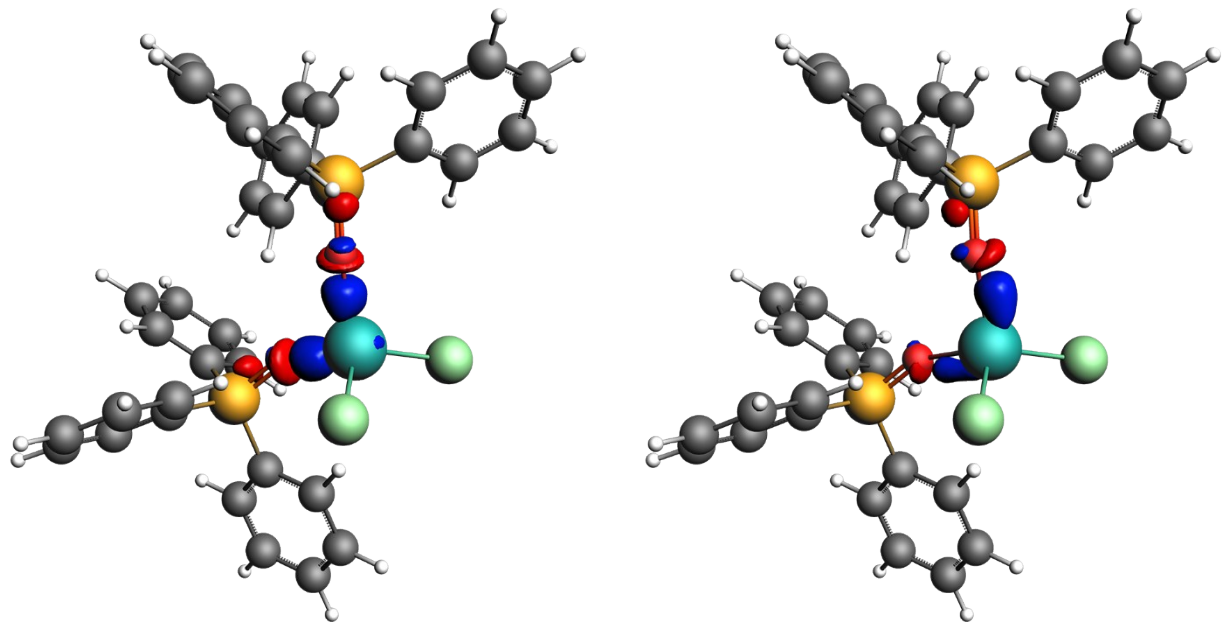


Fig. S45. The calculated deformation density $\Delta\rho_i$ (α -spin) for the $[(\text{Ph}_3\text{PO})_2\text{MnCl}_2]$ molecule formation from the two $\{\text{Ph}_3\text{PO}\}_2$ fragments and $\{\text{MnCl}_2\}$ fragment of **1** with NOCV eigenvalues: left-top – $|V| = 0.2776$; right-top – $|V| = 0.1712$; left-bottom – $|V| = 0.0985$; right-bottom – $|V| = 0.0904$. Red for $\Delta\rho_i < 0$ and blue for $\Delta\rho_i > 0$.



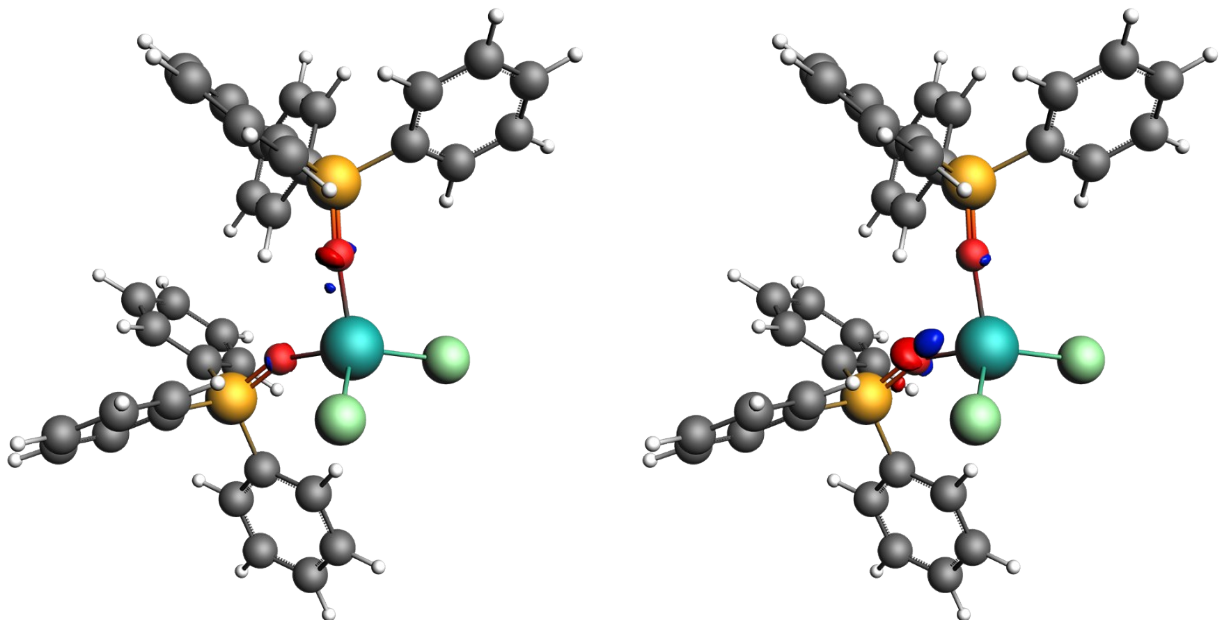


Fig. S46. The calculated deformation density $\Delta\rho_i$ (β -spin) for the $[(\text{Ph}_3\text{PO})_2\text{MnCl}_2]$ molecule formation from the two $\{\text{Ph}_3\text{PO}\}_2$ fragments and $\{\text{MnCl}_2\}$ fragment of **1** with NOCV eigenvalues: left-top – $|V| = 0.1900$; right-top – $|V| = 0.1552$; left-bottom – $|V| = 0.1340$; right-bottom – $|V| = 0.1279$. Red for $\Delta\rho_i < 0$ and blue for $\Delta\rho_i > 0$.

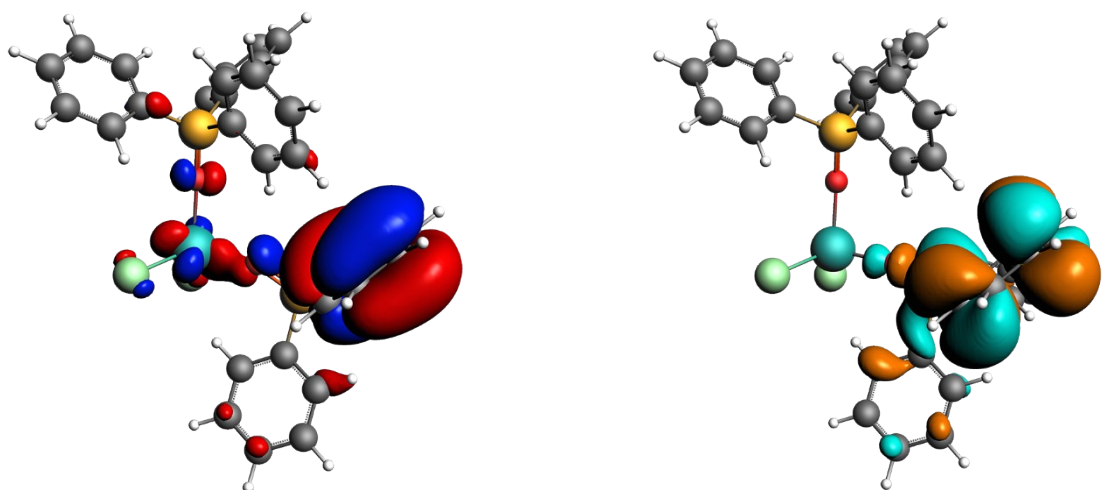


Fig. S47. Occupied (HOMO-20) (left) and unoccupied (LUMO) (right) α -spin orbitals of the $[(\text{Ph}_3\text{PO})_2\text{MnCl}_2]$ involved to the singlet-singlet excitation (transition number 2) using CAM-B3LYP functional.

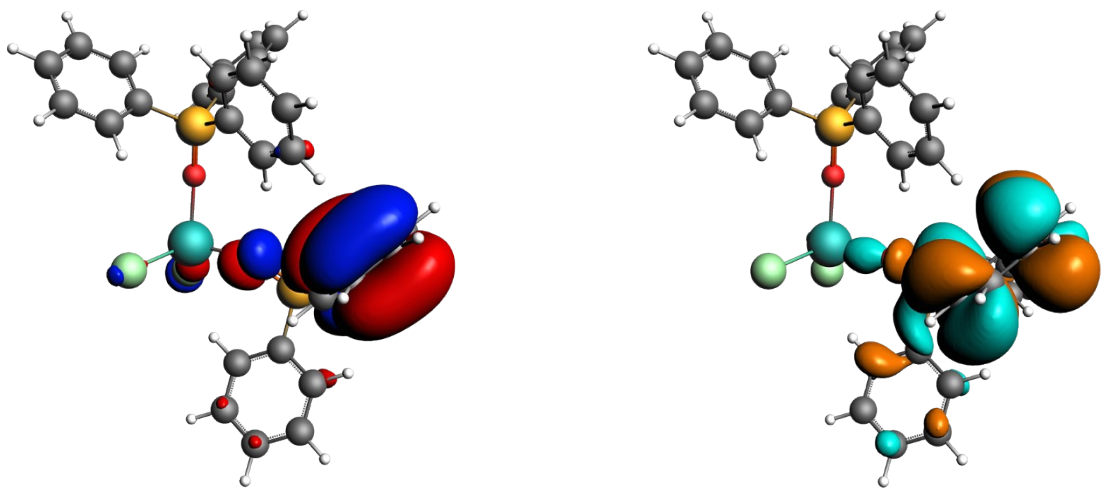


Fig. S48. Occupied (HOMO-17) (left) and unoccupied (LUMO) (right) β -spin orbitals of the $[(\text{Ph}_3\text{PO})_2\text{MnCl}_2]$ involved to the singlet-singlet excitation (transition number 2) using CAM-B3LYP functional.

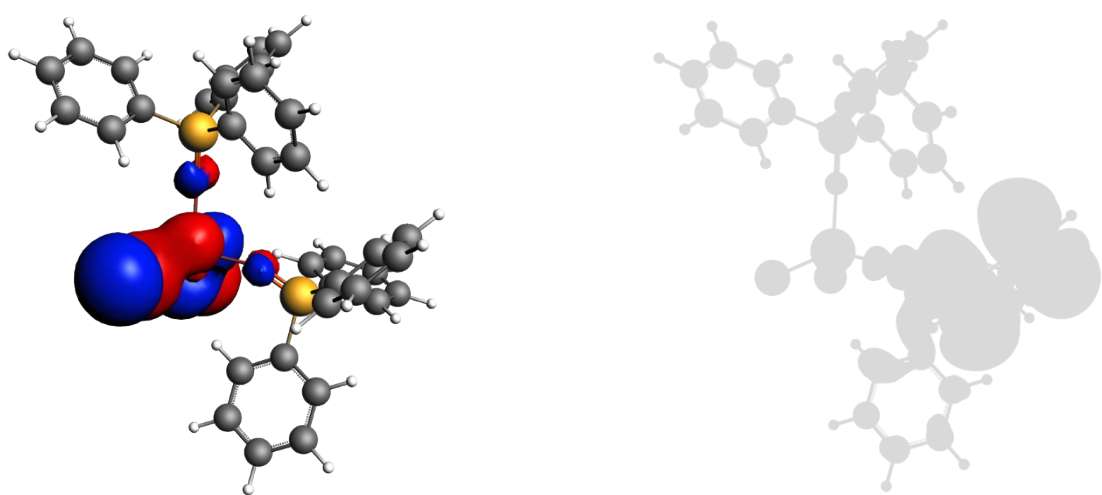


Fig. S49. Occupied (HOMO) (left) and unoccupied (LUMO) (right) α -spin orbitals of the $[(\text{Ph}_3\text{PO})_2\text{MnCl}_2]$ involved to the singlet-singlet excitation (transition number 7) using CAM-B3LYP functional.

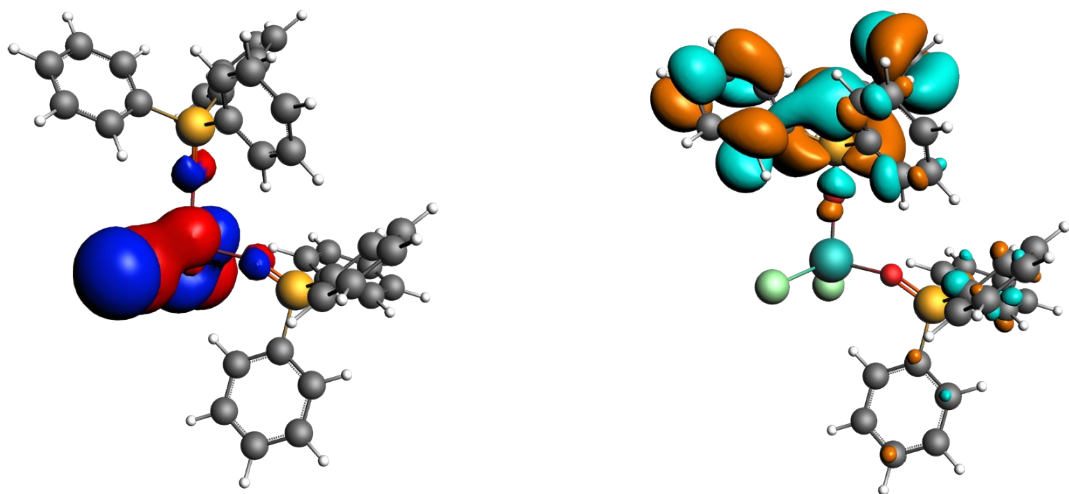


Fig. S50. Occupied (HOMO) (left) and unoccupied (LUMO+3) (right) α -spin orbitals of the $[(\text{Ph}_3\text{PO})_2\text{MnCl}_2]$ involved to the singlet-singlet excitation (transition number 14) using CAM-B3LYP functional.

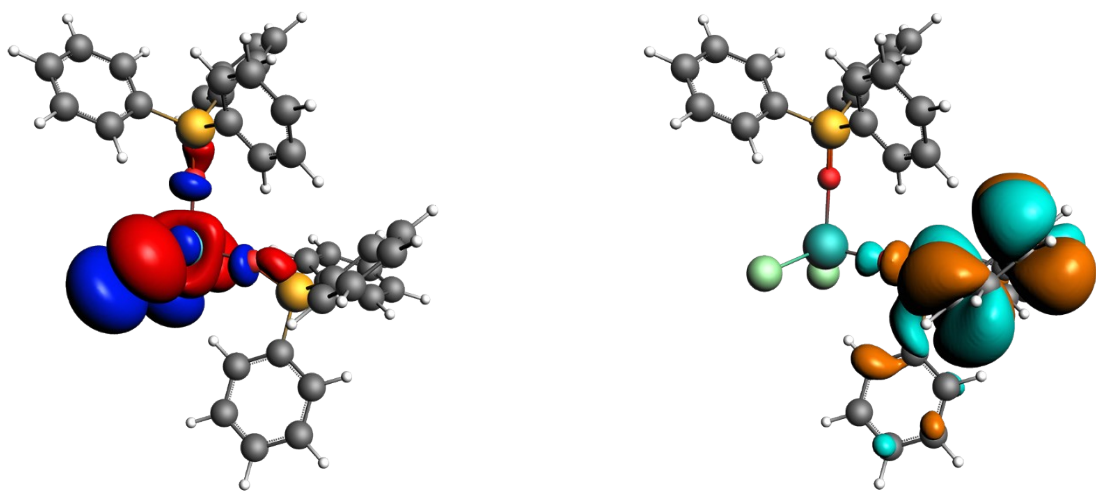


Fig. S51. Occupied (HOMO-1) (left) and unoccupied (LUMO) (right) α -spin orbitals of the $[(\text{Ph}_3\text{PO})_2\text{MnCl}_2]$ involved to the singlet-singlet excitation (transition number 16) using CAM-B3LYP functional.

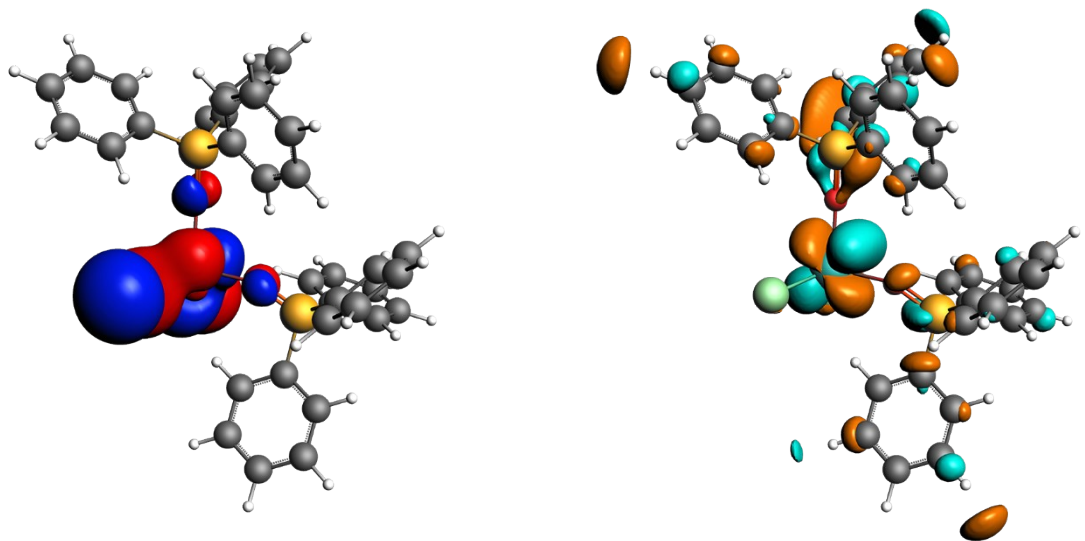


Fig. S52. Occupied (HOMO) (left) and unoccupied (LUMO+23) (right) orbitals of the $[(\text{Ph}_3\text{PO})_2\text{MnCl}_2]$ involved to the spin-flip transition (number 1) using CAM-B3LYP functional.

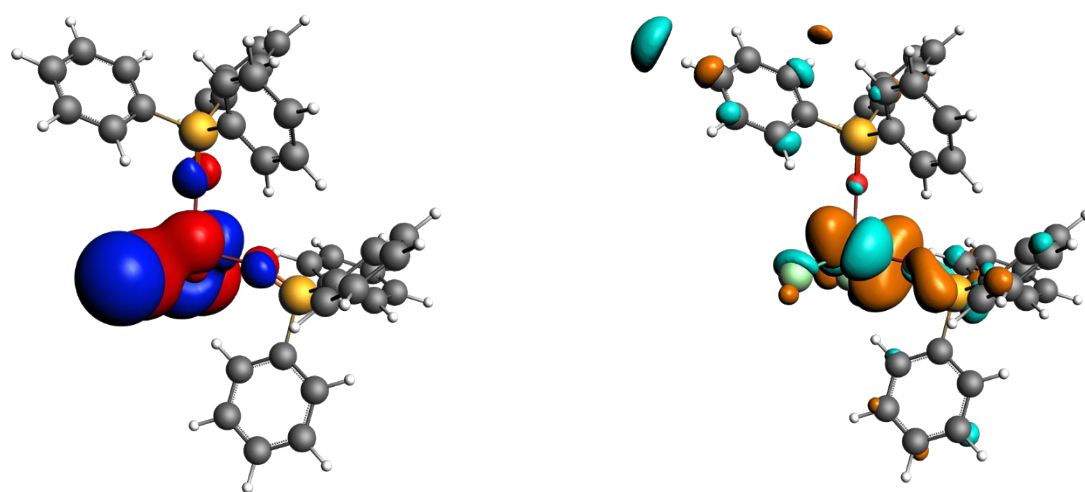


Fig. S53. Occupied (HOMO) (left) and unoccupied (LUMO+25) (right) orbitals of the $[(\text{Ph}_3\text{PO})_2\text{MnCl}_2]$ involved to the spin-flip transition (number 1) using CAM-B3LYP functional.

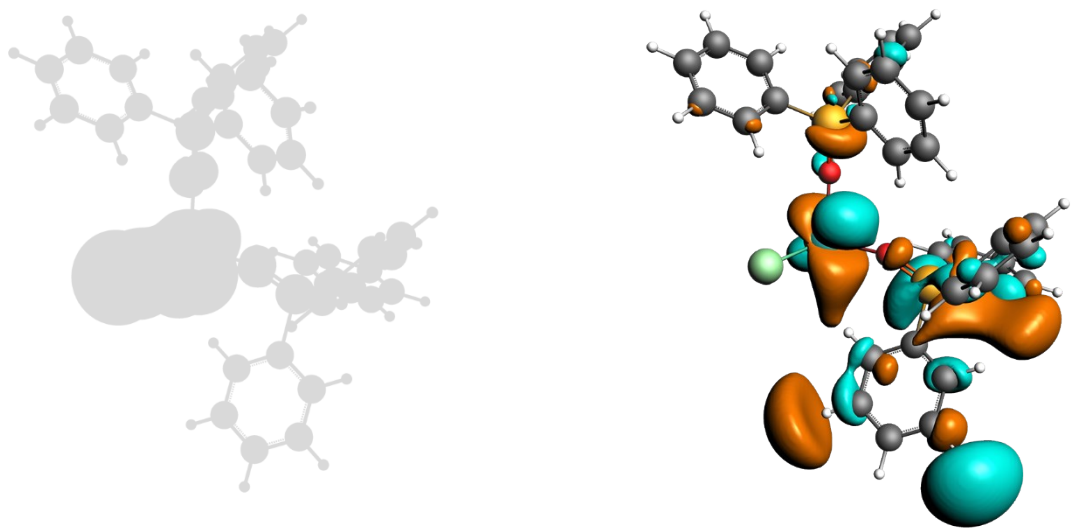


Fig. S54. Occupied (HOMO) (left) and unoccupied (LUMO+21) (right) orbitals of the $[(\text{Ph}_3\text{PO})_2\text{MnCl}_2]$ involved to the spin-flip transition (number 1) using CAM-B3LYP functional.

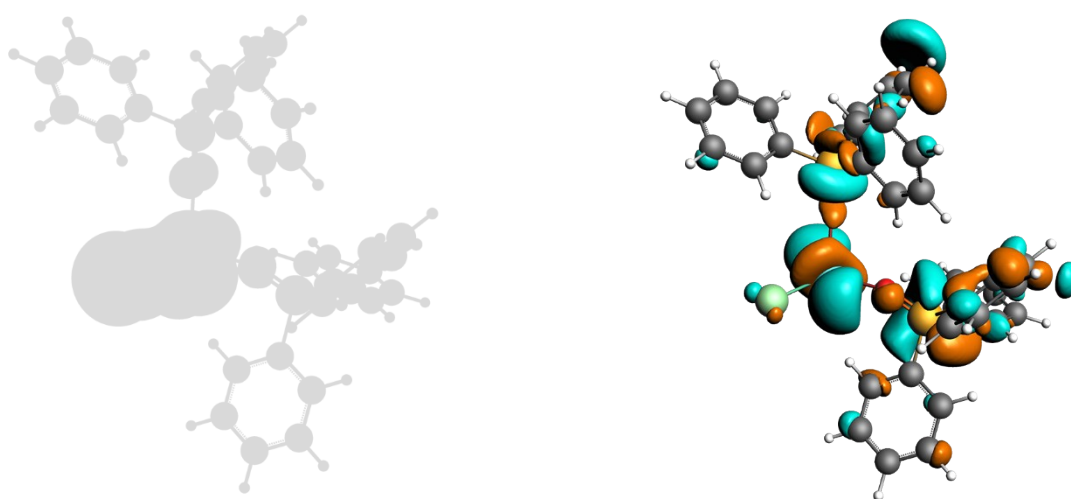


Fig. S55. Occupied (HOMO) (left) and unoccupied (LUMO+22) (right) orbitals of the $[(\text{Ph}_3\text{PO})_2\text{MnCl}_2]$ involved to the spin-flip transition (number 2) using CAM-B3LYP functional.

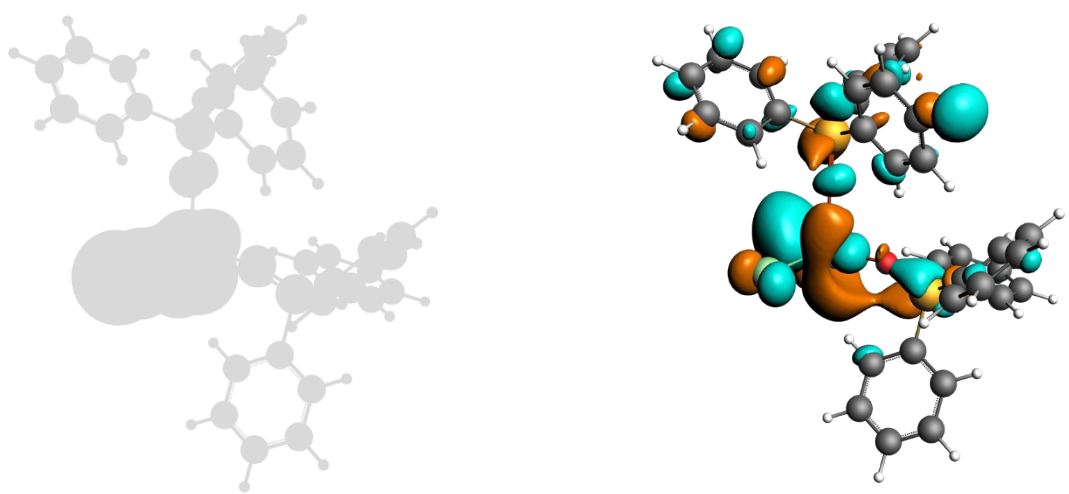


Fig. S56. Occupied (HOMO) (left) and unoccupied (LUMO+29) (right) orbitals of the $[(\text{Ph}_3\text{PO})_2\text{MnCl}_2]$ involved to the spin-flip transition (number 9) using CAM-B3LYP functional.

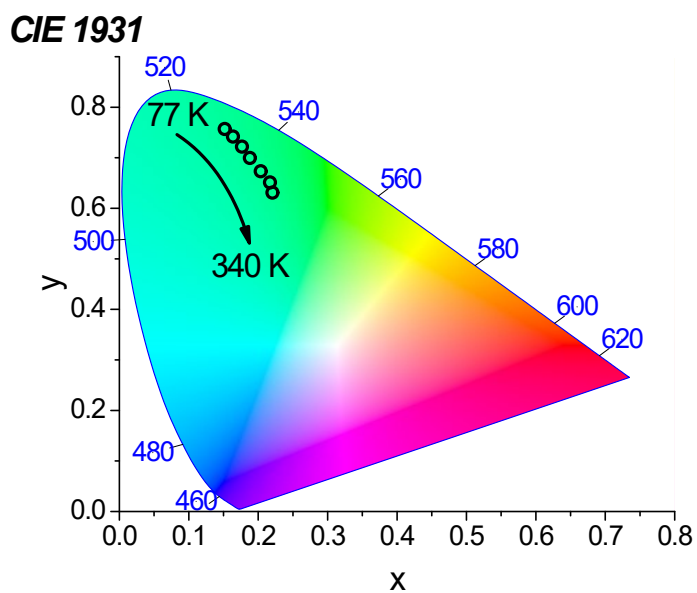


Fig. S57. Temperature dependences of the photoluminescence chromaticity of **1** ($\lambda_{\text{Ex}} = 275 \text{ nm}$).

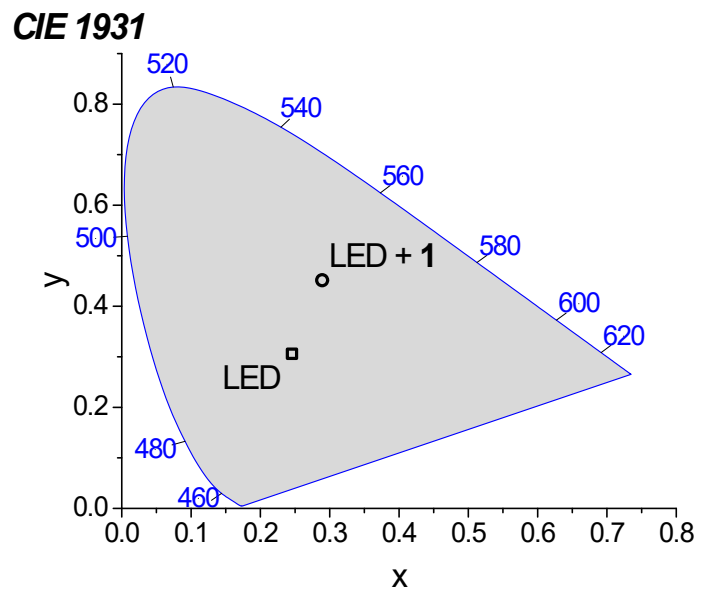


Fig. S58. Chromaticity of LED emission and photoluminescence of **1** excited by LED with $\lambda_{\text{max}} = 275$.